國立臺灣大學工學院土木工程學系大地組

碩士論文

Department of Civil Engineering

College of Engineering

National Taiwan University

Master's Thesis

海底電纜沖刷的物理模型

Physical modeling of Scouring of Submarine Cables

謝元舜

Yuan-Shan Hsieh

指導教授：郭安妮 博士

Advisor: Annie On-Lei Kwok, Ph.D.

中華民國 113 年 7 月

July, 2024

doi:10.6342/NTU202404035

doi:10.6342/NTU202404035

摘要

台灣是一個海島國家，由於陸地的空間資源有限，因此海洋空間的利用與發展尤為重要，近年來隨著海上風力發電的發展，海底電纜在沿海和近海工程中的重要性而受到廣泛的研究。當海底電纜暴露於直接水流作用時，電纜周圍會產生沖刷，這導致電纜的自由跨度懸空，增加應力和結構疲勞，因此研究海底電纜的沖刷行為有著其重要的意義。

對於電纜沖刷涉及波-海床-管線互制行為，我們試圖透過水槽實驗僅透過波浪來研究此類行為，實驗中我們利用不同的波浪角度，水深及埋深來對電纜進行沖刷，將實驗中產生的沖刷坑和沙丘紋利用石膏固定形狀，並利用 Agisoft metashape standard 進行近景攝影建立點雲，且使用 cloud compare 分析造成沖刷坑的深度及形狀。試圖去了解波浪角度對沖刷造成的影響。

關鍵字: 電纜、沖刷、水槽試驗、波浪方向、沙波紋

doi:10.6342/NTU202404035

Abstract

Taiwan is an island country with limited land resources, hence it is crucial to develop and utilize the surrounding maritime space. In recent years, with the on-going construction of offshore wind power generation, the performance of submarine cables is of great concern. When submarine cables are exposed to ocean waves and currents, scouring may occur around the cables, which may lead to dangling, increase in stress and structural fatigue of the cables. Therefore, studying the scouring behavior of submarine cables holds significant importance.

In this research, a series of flume experiments were performed to study the interaction between seabed sediment, pipe and wave action. In the tests, influence of the orientation of the pipe relative to the direction of the wave, water depth and burial depth of the pipe on scouring was examined. After the wave actions ceased, gypsum power was poured onto the surface of the sediment to stabilize the size and shape of the scour holes. As the gypsum solidified, close-range photogrammetry modeling was performed on the gypsum model to obtain 3D digital models and analyze the geometry of the scouring.

Keywords: cable, scour, flume test, wave direction, sand ripple

doi:10.6342/NTU202404035

doi:10.6342/NTU202404035

Table of Contents

doi:10.6342/NTU202404035

doi:10.6342/NTU202404035

List of Figures

doi:10.6342/NTU202404035

doi:10.6342/NTU202404035

doi:10.6342/NTU202404035

doi:10.6342/NTU202404035

List of Tables

doi:10.6342/NTU202404035

Chapter 1 Introduction

1.1 Motivation

Submarine cables play an irreplaceable role in marine engineering for offshore wind power generation. These cables, laid on the seabed, are subjected to scouring due to waves, ocean currents, and earthquakes, resulting in cable degradation and reduced lifespan.

The study of submarine cable scouring falls within the realm of wave-pipeline-soil interaction. After experiencing the scouring, there would be scour holes and span shoulders (Sumer and Fredsøe, 2002). Experimental research typically involves small-scale laboratory flume tests to measure the scour profiles near the pipelines. It has been found that the equilibrium scour depth depends on parameters such as flow velocity, pipe diameter (D), flow depth, initial gap (e) between the bed layer and the pipeline, and median grain size (d50). Most early studies were conducted through physical modeling, yielding numerous empirical formulas for scour depth. However, research on the direction of wave propagation and cable orientation is scarce.

1.2 Objectives of this Study

Hydraulic model testing involves scaling down a prototype to a model of certain

doi:10.6342/NTU202404035

geometric proportions to simulate flow phenomena around underwater structures and the hydraulic characteristics of seabed material transport in water. Compared to numerical simulation methods, hydraulic model testing provides a more tangible grasp of actual hydraulic conditions, flow patterns, and sediment transport phenomena. In this study, dimensionless (similarity) parameters are first evaluated to simulate specific field conditions. As for the wave velocity, while particle image velocimetry (PIV) is commonly used in typical flume experiments, linear wave theory is employed to compute the water particle trajectory velocities. Due to limitations in the size of the flumes, Reynolds number scaling is not conducted in the current tests. In most sediment transport models, if the Reynolds number (based on water depth) exceeds 10,000 in both model and prototype cases, the Reynolds number effect can be disregarded, which is a common practice in most sediment transport models.

This study aims to utilize physical models to understand the morphology of scour holes left by cable scouring. For the flume tests employed in this study, a flat seabed surface without any initial slope is used. The cable remains stationary, without deformation, movement, or vibration, and is only subjected to the wave action. After the wave actions cease, gypsum power is poured onto the surface of the sediment to stabilize the size and shape of scour holes. After the gypsum solidifies 3D scanning and close-

doi:10.6342/NTU202404035

range photogrammetry modeling are performed on the gypsum model.

For modeling purposes, we utilize Agisoft Metashape Standard for close-range photogrammetry to generate point clouds and employ Cloud Compare to analyze the depth and shape of scour holes. The influence of wave characteristics and pipe location on the scouring geometry is studied.

1.3 Organization of this Thesis

This thesis contains five chapters. In Chapter 1, motivation and objective of the current research work are presented. In Chapter 2, past studies on scouring are reviewed. In Chapter 3, experimental setup of the flume tests is introduced. In Chapter 4, experimental results and close-range photogrammetry analyses are discussed. Lastly in chapter 5, summary of research findings and recommendations for future studies are given.

doi:10.6342/NTU202404035

Chapter 2 Literature Review

Because cables are highly similar to submarine pipelines and there are limited studies on the scourng of submarine cables, the literature review on submarine pipelines is presented in this chapter.

2.1 Mechanism of Scour

2.1.1 Seepage flow underneath the cable

When cables are laid on a sediment bed and subjected to wave action, seepage flow occurs beneath the cables, leading to the formation of a pipe that carries soil from the channel, ultimately resulting in scour holes, a phenomenon known as piping. Waves passing over the cables create a pressure differential on either side of the cables, as depicted in Figure 2.1. When this pressure differential reaches a critical point, a mixture of sand and water is expelled to the surface, forming a channel. Previous studies have regarded piping as the primary mechanism responsible for the onset of scour below pipelines.

Sumer et al. (2001) piping occurs in cohesionless granular materials when the pressure gradient $\frac{\partial}{\partial x}\left(\frac{p}{\gamma}\right)$ exceeds the flotation gradient (s-1)(1-n):

doi:10.6342/NTU202404035

$$\frac{\partial}{\partial x}\left(\frac{p}{\gamma}\right) \geq (s-1)(1-n) \qquad (2.1)$$

where $\frac{\partial p}{\partial x}$ represents the pressure gradient driving the seepage directly below the pipe, s is the specific gravity of sand, γ is the specific gravity of water, and n is the porosity. During piping, the soil at the outlet loses internal shear strength.

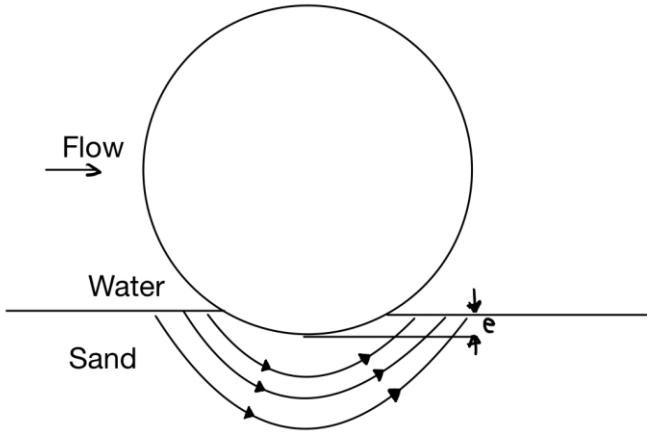

Figure 2.1 Schematic diagram of seepage flow underneath the cable

2.1.2 Criterion of Scour

Sumer et al. (1991) proposed an equation for the criterion of the onset of scour, which can be expressed in the following non-dimensional form:

$$\left(\frac{U^2}{gD(1-n)(s-1)}\right)_{cr} \geq f(\frac{e}{D}) \qquad (2.2)$$

where U is wave velocity, g is acceleration due to gravity, s is the specific gravity of

doi:10.6342/NTU202404035

sand, n is porosity,the function f(e/D) is to be determined from experiments. It may be noted that f is a function of not only the gap-to-diameter ratio, e/D. In wave conditions, the equation can be applied under the following conditions:

Replace U with U_m, the maximum orbital velocity of water particles.

Regarding the function, there will be an additional parameter, namely f(e/D, KC). Sumer and Fredsøe (1991) discussed the dependency of the onset of scour on KC in their study. In their research, as both e/D and KC increase, the critical value of the parameter) $\frac{U_m}{gD(1-n)(s-1)}$ also increases, where KC is the Keulegan-Carpenter number had been told in afterword.

Another parameter relevant to the onset of scour is the critical shields parameter, θ_{cr}. The shields parameter essentially represents the ratio between the gravitational force acting on sediment particles and the drag force exerted by the fluid flow. It helps predict whether sediment particles will be entrained and transported by fluid flow or remain stationary.

$$\theta = \frac{U_m^2}{g(s-1)d_{50}} \tag{2.3}$$

where U_m is the maximun value of the orbital velocity at the bed, g is gravity acceleration, s is the specific gravity of sand, d_{50} is mean particle size of sand. For wave scour, the

doi:10.6342/NTU202404035

maximum bed friction velocity U_{mf} instead of U_m is used to calculate the value of θ by (2.3)

Zhang et al. (2016):

$$U_{mf} = \sqrt{\frac{f_w}{2}} U_m \tag{2.4}$$

where U_m is the maximum orbital velocity of water particles at the seabed; and f_w is the friction factor for the wave boundary layer, assuming the bed is a rough boundary.

Fredsøe and Deigaard (1992):

$$f_w = 0.04 \left(\frac{\alpha}{k_s}\right)^{-\frac{1}{4}} \tag{2.5}$$

where k_s is equivalent sand rounghness of the bed, α is the amplitude of the orbital motion of water particles at the seabed and is given by

$$\alpha = \frac{U_m T_w}{2\pi} \tag{2.6}$$

When the shields parameter reaches its critical value, sediment transport begins. Below this critical value, sediment particles are typically stationary. The critical shields parameter depends on various factors such as particle size distribution, sediment shape, and flow conditions.

For different rivers and riverbeds, the numerical value of the critical shields

doi:10.6342/NTU202404035

parameter may vary. An empirical formula had been proposed to estimate the critical shields parameter:

$$\theta_c = 0.047 + 0.065\left(\frac{d_{50}}{D}\right)^{0.6} \quad (2.7)$$

Where d_{50} is mean particle size of sand, D is pipeline diameter.

2.2 Theoretical Study of Scour

2.2.1 Self-burial of Cable

After the scour initiates beneath the cable, it propagates along the cable's length. As the process continues, the length of the free span increases while the stretches of soil, known as span shoulders, where the cable obtains support, decrease. Consequently, the weight of the cable increasingly rests on shorter lengths of the span shoulders. This process may reach a level where the soil's bearing capacity is exceeded, leading to soil failure. Failure occurs as sliding in two outward directions, a type of failure known as general shear failure in soil mechanics. As shown in Figure 2.2 Clearly, with continued scouring, as the bearing area continually reduces, the soil's bearing capacity will be continually exceeded, resulting in permanent subsidence of the cable. This process only ceases when the cable subsides to a depth sufficient to withstand scouring. Once scouring stops, the ongoing soil failure halts, and consequently, the cable's subsidence stops as well.

doi:10.6342/NTU202404035

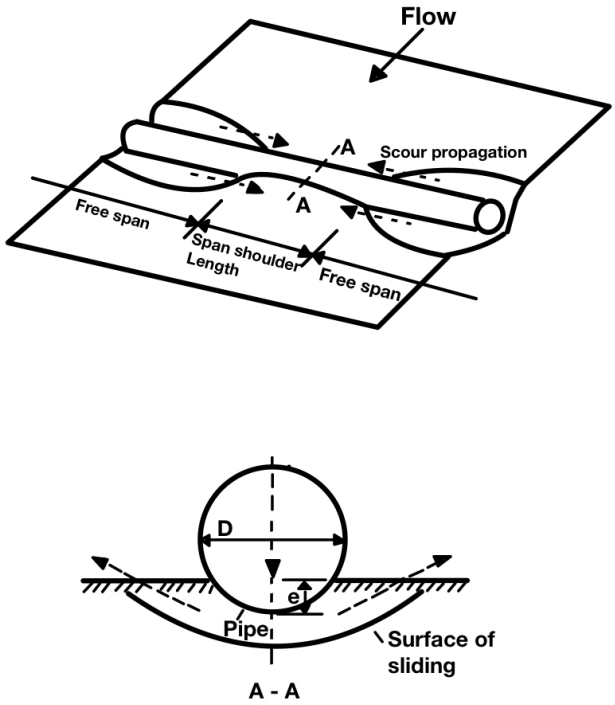

Figure 2.2 Definition stetch. Sinking of cable at span shoulder (Sumer et al. 2001).

As mentioned in the previous paragraph, the scour depth is closely related to KC and e/D. Numerous predecessors have proposed equations for estimating scour depth (Sumer, et al. 2001, Cevik & Yuksel 1999, Li & Ma 2022, Pu, et al. 2001, Mousavi, et al. 2009, Etemad-Shahidi et al. 2011, Sharafafi et al. 2018), and pointed out that if the buried depth of the pipeline exceeds the scour depth, scour will not occur.

Sumer et al. (2001) proposed:

doi:10.6342/NTU202404035

$$\frac{S}{D} = 0.1\sqrt{KC} \tag{2.8}$$

This applies to pipes without burial depth.

Cevik & Yuksel (1999) :

$$\frac{S}{D} = 0.11 * KC^{0.45} \tag{2.9}$$

Li & Ma (2022):

$$0.13 * \exp\left(-\frac{1.8e}{D}\right) \geq S(e, D) \geq 0.09 * \exp(-\frac{2.1e}{D}) \tag{2.10}$$

Pu et al. (2001):

$$\frac{S}{D} = B * KC^{m} \tag{2.11}$$

m = 3.18 for a sandy bed, and B is a function of KC and $\frac{e}{D}$

$$\frac{e}{D_{cr}} = 2.2 \log KC - B \tag{2.12}$$

Mousavi et al. (2009):

$$\frac{S + |e|}{D} = 0.1KC^{0.5}\ ,\ KC < 6 \tag{2.13}$$

Etemad-Shahidi et al. (2011):

$$\frac{S}{D} = 3.344KC^{0.512}\theta^{1.296} \exp\left(-\frac{2.32e}{D}\right),\ \theta \leq 0.064$$

$$\frac{S}{D} = \begin{cases} 0.149KC^{0.477}\theta^{0.121} \exp\left(-\frac{0.472e}{D}\right),\ \theta > 0.064, \frac{e}{D} \leq 0.145 \\ 0.149KC^{0.782}\theta^{0.121} \exp\left(-\frac{0.942e}{D}\right),\ \theta > 0.064, \frac{e}{D} > 0.145 \end{cases} \tag{2.14}$$

doi:10.6342/NTU202404035

Sharafafi et al. (2018):

$$\frac{S}{D} = 4.17KC^{0.72}\theta^{1.55}\exp\left(-\frac{3.9e}{D}\right),\ \theta \le 0.064$$

$$\frac{S}{D} = \begin{cases} 0.149KC^{0.42}\theta^{0.08}\exp\left(-\frac{0.472e}{D}\right),\ \theta > 0.064, \frac{e}{D} \le 0.145 \\ 0.073KC^{0.45}\theta^{0.17}\exp\left(-\frac{0.094e}{D}\right),\ \theta > 0.064, \frac{e}{D} > 0.145 \end{cases} \quad (2.15)$$

Zang et al. (2019):

$$\frac{S}{D} = 0.929\left(\frac{U^2}{2gD}\right)^{0.26}\left(\frac{d_{50}}{D}\right)^{-0.04} \quad (2.16)$$

where S is scour depth, D is pipeline diameter, g is acceleration due to gravity, U is wave velocity, d_{50} is mean particle size, e is embedment depth, θ is shields parameter. Mousavi (2009) also basis on their data and proposed the equation to predict the relationship between scour depth and scour width.

$$\frac{W_t}{D} = 7\left(\frac{S}{D}\right)^{0.6} \quad (2.17)$$

Where W_t is the total scour width.

The most famous one is (2.8) published by Sumer et al. Figure 2.2 shows the comparison between previous experiments and (2.8). It can be seen that Sumer et al. published prediction equations and other previous data. consistent, and the direction of the data is also consistent.

doi:10.6342/NTU202404035

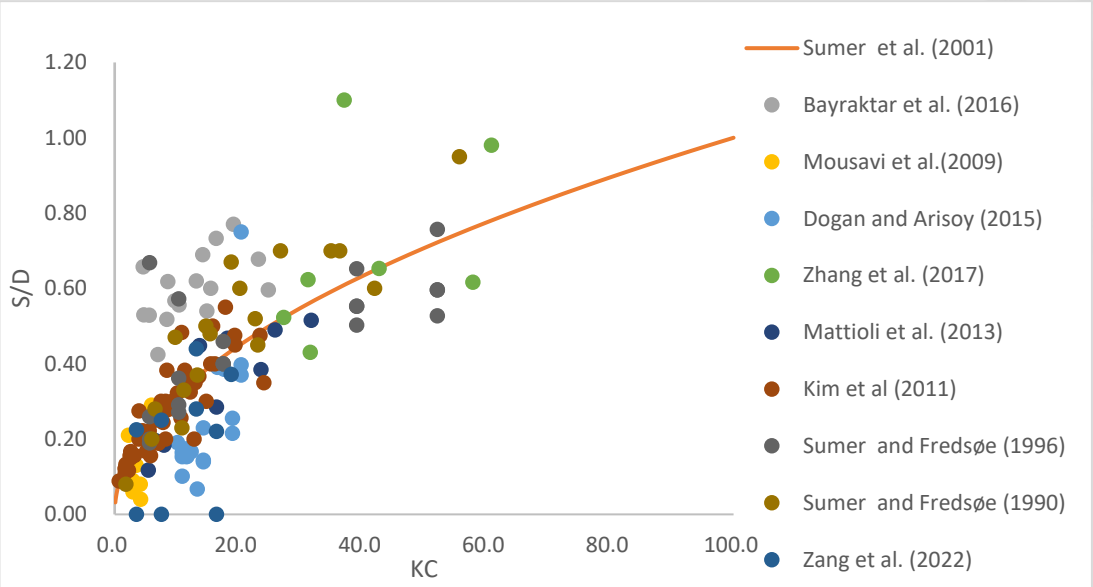

Figure 2.3 Data of wave-induce scour depth

2.2.2 Effect of Pipeline Angle

Zang et al. (2019) Established a new relationship to reflect the influence of burial depth and pipeline direction. The relationship is established based on the theory proposed by Mohr et al. (2016), where the equilibrium depth is proportional to the control volume below the pipe. Therefore, the equilibrium depth of a pipe with embedding depth and incident flow angle can be expressed as (2.18).

$$\frac{S}{S_0} = \gamma_1^{\alpha 1}\gamma_2^{\alpha 2} \tag{2.18}$$

S_0 is the scour depth perpendicular to the wave direction of the pipe. S is the scour depth of pipes at other angles under the same wave strip. It can be calculated through known empirical formulas. If it is a wave-only condition, use (2.8). Buried The influence of depth

doi:10.6342/NTU202404035

on the control volume can be reflected by the coefficient γ_1. The control volume has a value of D for e/D=0 and α=0, can be drawn by (2.19). The coefficient γ_2 represents the relationship between the flow incident angle and the influence of control volume can be expressed as (2.20)

$$\gamma 1 = \sqrt{1 + 4\left(\frac{e}{D}\right)^2} \tag{2.19}$$

$$\gamma 2 = \frac{1}{\cos\alpha} \tag{2.20}$$

$\alpha 1$ and $\alpha 2$ are empirical coefficients and can be determined based on experimental results. Curve fitting was performed through the experimental results. The values of $\alpha 1$ and $\alpha 2$ in the study by Zang et al. were -1.10 and -0.90 respectively.

doi:10.6342/NTU202404035

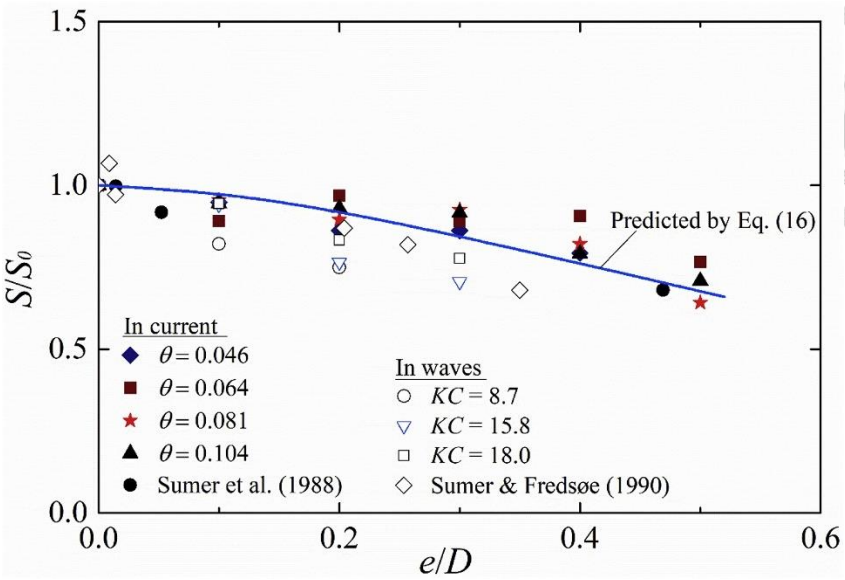

Figure 2.4 Effect of the embedment depth on the equilibrium depth for $\alpha = 0°$.(Zang et al.2019)

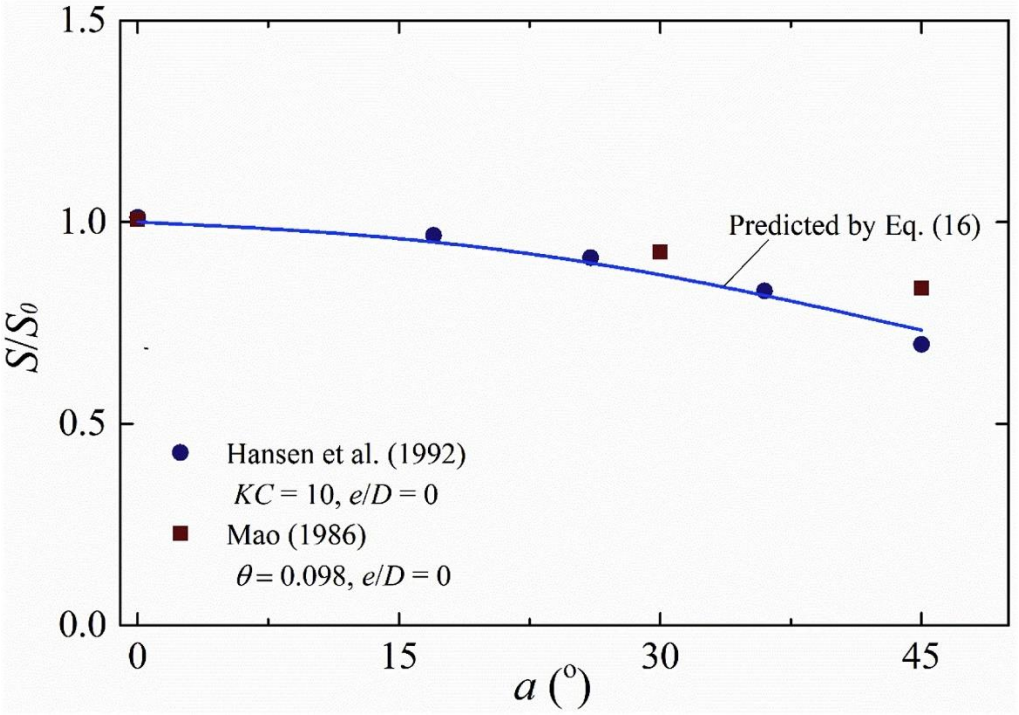

Figure 2.5 Effect of the flow incident angle on the equilibrium depth for $e/D = 0$ (Zang et al.2019)

doi:10.6342/NTU202404035

Figure 2.4 shown is the variation of S/S_0 with e/D when α = 0° (i.e. γ2 = 1.0). It is obvious that when e / D = 0, the value of S/S_0 is 1.0. Wave condition data from Sumer and Fredsøe (1990) are plotted in the figure. The results of the present experiments are also compared. It can be seen that as e/D increases from 0 to 0.5, S/S_0 decreases from 1.0 to about 0.65. This is mainly because as the burial depth increases, the amplification coefficient of the bed shear stress under the pipeline decreases, resulting in a decrease in the bed shear stress, which in turn leads to a reduction in sediment transport within the punching hole.

Detailed comparison of experimental results with equilibrium depth predictions for other values of e/D and α, Figure 2.5 shows the variation of $S/S_0$with α under current and wave conditions when e/D = 0 (i.e. γ_1= 1.0). Therefore, at α = 0°, the value of S/S_0 is 1.0. As α increases from 0° to 45°, S/S_0 decreases from 1.0 to about 0.70. This can be explained by the fact that the forward component of the flow incident on the pipe contributes most to the development of scour, and therefore the effective bed shear stress transported by the sediment below the pipe decreases with the increase of the water flow incidence angle.

2.3 Experimental Study on Scouring

Three different physical experimental methods have been employed in previous

doi:10.6342/NTU202404035

studies: wave flume tests, compression tests, and centrifuge wave tests. Among these methods, wave flume tests are most commonly used because experiments can be well controlled to obtain relatively accurate measurement data.

Due to the uncertainty of marine conditions, it is crucial to design the size of the seabed, structures, and waves according to scale laws. However, scale effects have always been a concern in laboratory experiments. Due to limited experimental space and complex model fabrication conditions, it is necessary to determine the proportional geometric quantities between the prototype and the model in model design.

Due to the drawback of wave flume tests in simulating the stress levels of the seabed, and the absence of scale laws adapted to seabed sediments in existing studies, the model is considered a small-scale prototype. To simulate interactions in experiments, three dimensionless numbers related to flow characteristics can be derived, including the Froude number (Fr), Keulegan-Carpenter number (KC), and Reynolds number (Re). In the real marine environment, gravity dominates the motion of waves and currents, while viscous and inertial forces are too small to significantly affect fluid motion. Therefore, viscosity and inertia are typically disregarded in scale laws, i.e., the Reynolds number.

The Froude similarity is commonly applied in wave flume tests, expressed as:

doi:10.6342/NTU202404035

$$F_r = \frac{U_m}{(gD)^{\frac{1}{2}}} \tag{2.21}$$

where g denotes the gravity acceleration, D denotes the hydraulic radius, and Um denotes the wave orbital particle velocity near the seabed.

The other dimensionless numbers are as follows:

$$KC = \frac{U_m T}{D} \tag{2.22}$$

where T is the wave period.

The physical significance of the Keulegan-Carpenter number lies in its description of the influence of fluid loads on structures relative to the size of the structures and flow characteristics. When the Keulegan-Carpenter number is large, it means that the cyclic load endured by the structure is large, which may cause structural vibration, fatigue, and damage. On the contrary, when the Keulegan-Carpenter number is small, the effect of cyclic loading on the structure is relatively small. According to Froude similarity, it can be expressed as:

$$\frac{\lambda_{U_m}}{\lambda g^{\frac{1}{2}} \lambda_D^{\frac{1}{2}}} = 1 \tag{2.23}$$

In this equation, λ represents the ratio of model parameters to the prototype. Since all experiments are conducted under 1g conditions, λg=1, and the equation can be expressed as:

doi:10.6342/NTU202404035

$$\lambda_{U_m} = \lambda_D^{\frac{1}{2}} \tag{2.24}$$

The KC number can also be expressed as:

$$\frac{\lambda_{U_m}\lambda_T}{\lambda_D} \tag{2.25}$$

Combining equations (2.9) and (2.10) we get

$$\frac{\lambda_{U_m}\lambda_T}{\lambda_D} = \frac{\lambda_T}{\lambda_D^{\frac{1}{2}}} \tag{2.26}$$

Further simplification

$$\lambda_T = \lambda_D^{\frac{1}{2}} \tag{2.27}$$

(2.23) and (2.24) constitute the similarity between the laboratory

experimental model and the prototype.

Table 2-1 Part of Mousavi's experiment

Test NO.	water depth(cm)	H(cm)	T(s)	D(cm)	KC	Pipe initial depth(cm)	θ
W1	30	8.3	1.4	11	2.2	0	0.081
W12	30	7.7	1.4	11	4.13	2	0.101

Mousavi (2009) conducted several experiments, they presented the development of the wave-induced scour profile leading to the equilibrium stage when the pipe was

doi:10.6342/NTU202404035

scoured. Figure 2.7 depicts the various stages of scour profile development around the pipe, progressing from the initial to the fully developed stage in W1. They also provided a case where scour did not occur, W12.

Based on theory and their experimental data from W1, they proposed the following equation for predicting results that better fit the experimental outcomes:

From linear, Stokes, and cnoidal wave theories, the equation is derived to estimate the maximum velocity of water particle orbital motion at the bed:

$$U_m = \frac{\pi H}{T} \frac{1}{\sinh\left(\frac{2\pi h}{L}\right)} \tag{2.28}$$

As for the scour depth, bringing (2.28) into (2.8) we can get the following equation to predict scour depth.

$$S = 0.1 \sqrt{\frac{\pi H D}{\sinh\left(\frac{2\pi h}{L}\right)}} \tag{2.29}$$

doi:10.6342/NTU202404035

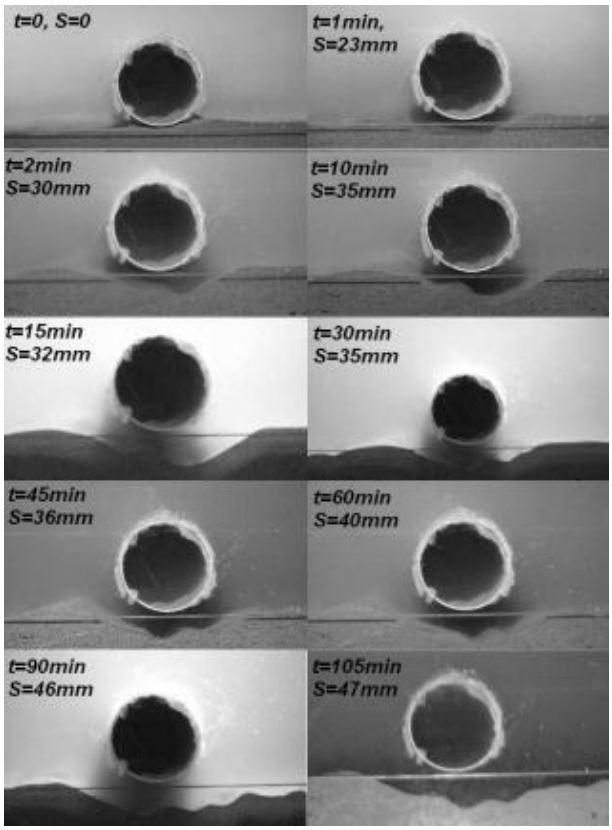

Figure 2.6 The development of wave-induce scour profile leading to the equilibrium stage in W1(Mousavi et al. 2009)

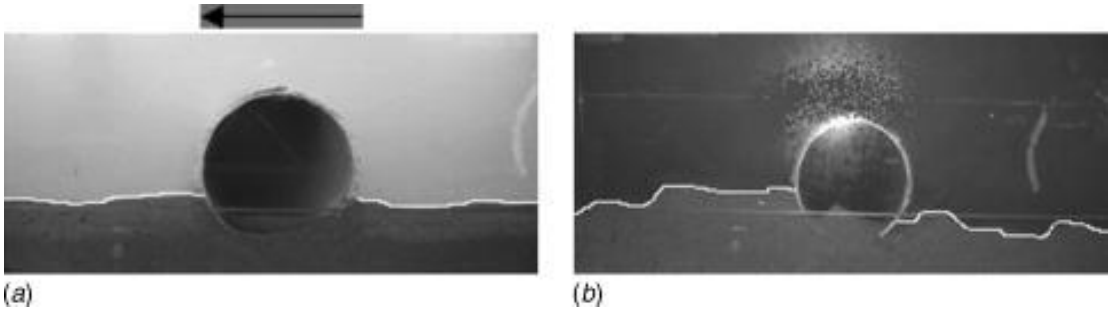

Figure 2.7 Test W12 (a)start of the test (b) end of the test. (Mousavi et al. 2009)

doi:10.6342/NTU202404035

2.4 Numerical Simulation

Ma et al. (2024) published a study using a CFD-DEM coupled model to investigate the scour mechanisms around pipelines under different ocean current conditions. Table 2-2 shows Ma et al. They used simulations to conduct a detailed analysis of fluid flow around the pipe, seepage through the sediment bed, and the drag force acting on the particles at different locations and times. They found that in addition to seepage, wakes can cause soil surface erosion. As shown in Figure 2.8, Ma et al. By analyzing the flow around the pipeline using a CFD-DEM coupled model, the erosion process around the pipeline was identified, including luff erosion, tunnel erosion and lee erosion. They discuss seepage and focus on the forces acting on particles, primarily related to the flow field affecting particle motion. In their study, the movement speed of water particles in the flow field under pure wave conditions was simulated, as shown in Figure 2.9. It can be observed that under pure wave conditions, the oscillating flow can be divided into two parts: one part is the forward flow and the other part is the backward flow. A leeward wake forms behind the pipe, causing scour-like changes to the seafloor surface.

doi:10.6342/NTU202404035

(a) shows the flow vectors around the pipe under pure wave conditions in the front stage. When forward flow passes through, the flow pattern around the pipe is very similar to pure water flow conditions with a wake.

(b) shows the simulation results for another case W2, where the pipe is fixed above the sediment bed and e/D=0.

Except for the different burial depths, the numerical model parameters of W1 and W2 are the same. It can be observed that under W2 conditions, the vortex intensity (e/D=0) around the pipe increases by more than 20%, which enhances the interaction between fluid and particles near the pipe.

Under wave conditions, the pressure field is related to water depth. Under wave conditions, water depth is constantly changing, causing pressure differences upstream and downstream to vary. Figure 2.10 shows the deep flow conditions around pipelines with different buried depths under pure wave conditions. It can be seen that compared with W1 with burial depth, W2 without burial (e/D=0) is more prone to tunnel erosion. Furthermore, in addition to directly below the pipe, regions with higher U_w can also be observed before and after the pipe, which may be due to the wake effect.

doi:10.6342/NTU202404035

Table 2-2 Simulations setups (Ma et al.)

Case	Ucur(m/s)	Uwave(m/s)	T(s)	h/D	e/D	KC	other parameters
C1	0.44	0		0	0.25	\	d=0.8mm
W1	0	0.06	4	2.4	0.25	4.8	H=0.3m
W2	0	0.06	4	2.4	0	4.8	D=0.05m
CW1	0.15	0.06	4	2	0.25	4	
CW2	0.18	0.06	4	2.4	0.25	4.8	

where U_{cur} is the flow velocity due to current, and U_{wave} is the wave orbital velocity, h is water depth, U_{cur} is the flow velocity due to current, and U_{wave} is the wave orbital velocity.

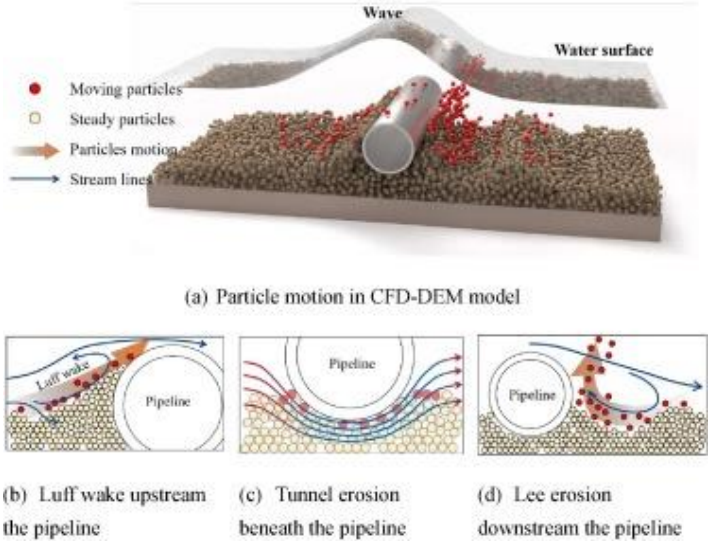

Figure 2.8 Scour mechanisms around the pipeline (Ma et al. 2024)

doi:10.6342/NTU202404035

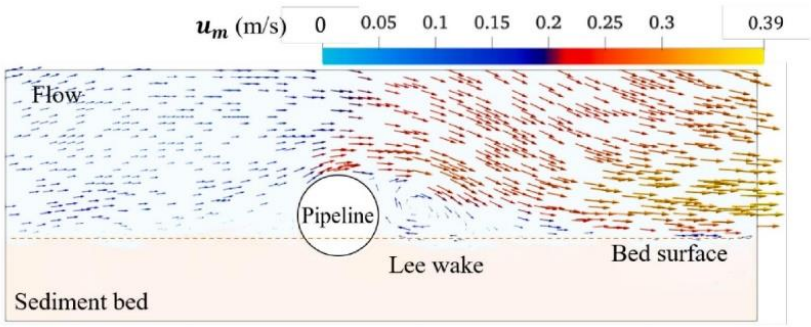

(a) Case W1 with the pipeline slightly sinking into the bed ($e/D = 0.25$)

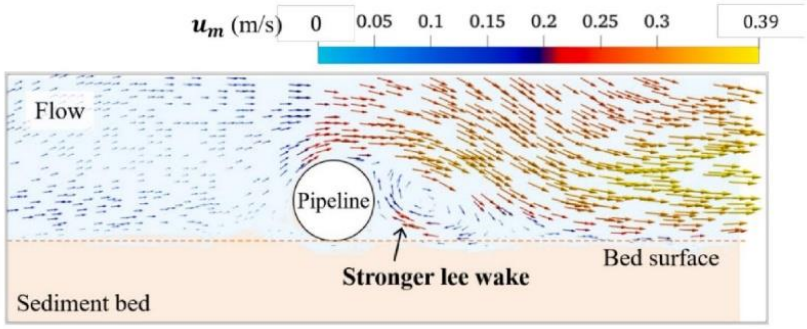

(b) Case W2 with the pipeline lying on the bed ($e/D = 0$)

Figure 2.9 Water particle velocities under wave only (Ma et al. 2024)

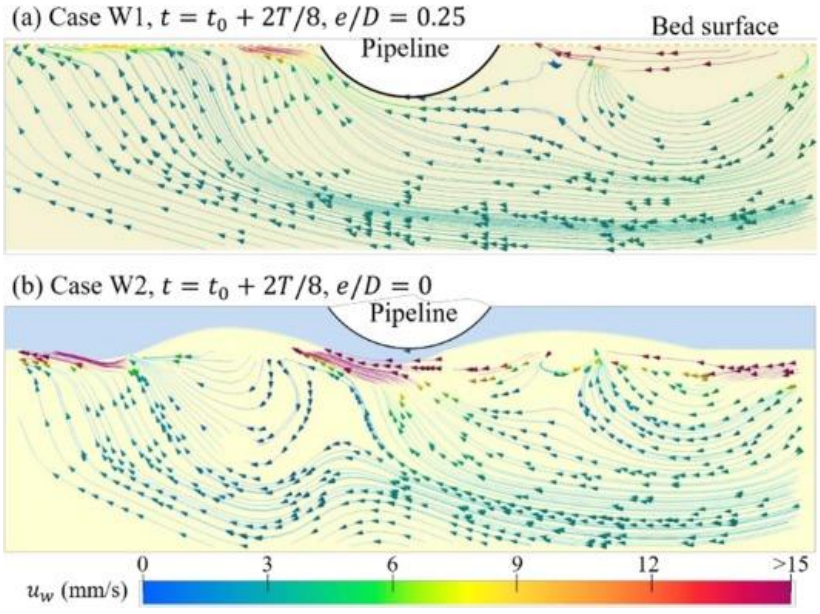

Figure 2.10 Seepage around pipelines at different burial depths under wave-only (Ma et al. 2024)

doi:10.6342/NTU202404035

2.5 Wave Ripple

Ripples are periodic patterns that appear on the seabed, characterized by dimensions typically on the scale of tens of centimeters. These bedforms are generated and sustained by the interaction between flowing seawater and non-cohesive sediments composing the bottom, usually sand. Ripples are genetically similar to sand waves, tidal ridges, and other forms observed along rivers, originating from the instability of flat bottom structures. This instability leads to the growth of bedforms of various lengths, depending on the characteristics of sand and water flow.

From the smallest ripples (centimeters long) to large riverbeds (kilometers long), there appears to be a continuum of bedform shapes. Despite being the smallest bedforms, ripples play a crucial role in many transport processes because flow typically separates at their crests, and the resulting vortices enhance momentum transfer, sediment transport, and general mixing phenomena.

Wave ripples are generated by the oscillatory motion of water caused by propagating or standing surface waves near the seabed. The lengths and heights of ripples are typically predicted using empirical formulas. It can be reasonably assumed that the

doi:10.6342/NTU202404035

geometric shape of ripples depends on the kinematic viscosity of seawater and the period of oscillation induced by surface waves near the bottom.

Nielsen (1981) proposed to predict the wavelength of the ripples by using (2.30)

$$\frac{\lambda_r}{\frac{U_0}{\omega}} = \exp\left(\frac{693 - 0.37\mathrm{In}^8\psi_d}{1000 + 0.75\mathrm{In}^7\psi_d}\right) \tag{2.30}$$

to predict the wavelength of the ripples observed in the field

$$\frac{\lambda_r}{\frac{U_0}{\omega}} = 2.2 - 0.345\psi_d^{0.34} \tag{2.31}$$

to predict the wavelength of the ripples generated by a regular oscillatory flow. Where ψ_d is the sediment mobility number given by

$$\psi_d = \frac{U_0^2}{(s-1)gd} \tag{2.32}$$

Where s is the relative density of the soil and water, d is mean grain size, g is gravity acceleration, $U_0 = \frac{a\omega}{\sinh\left(\frac{2\pi}{L}h\right)}$ is amplitude of the oscillations of the horizontal velocity component close to the bottom, $\omega = \frac{2\pi}{T}$ is the angular frequency of the sea waves, a is amplitude of the sea wave.

Soulsby and Whitehouse (2005) suggested using the following formula to predict wave ripple height h_r under the condition of known wavelength.

doi:10.6342/NTU202404035

$$\frac{h_r}{\lambda_r} = 0.15(1 - \exp(-\left(\frac{5.0 \times 10^3 d}{\frac{U_o}{\omega}}\right)^{3.5}))$$ (2.33)

doi:10.6342/NTU202404035

Chapter 3 Experimental Study

As Chapter 2 said, since cables are highly similar to submarine pipelines, we referred to the settings of submarine pipelines in the experimental part. In the experimental setting, we assume some conditions:

1. The cable does not deform and the potential vibration caused by the wave force acting on it is ignored.
2. We also ignore the difference in surface materials of cables and PVC pipes.
3. The seabed surface is flat without any slope
4. Ignore the current state and only consider waves

The actual experimental process is as shown in the flow chart below. The experimental process is divided into two parts. In addition to the flume test, some soil properties tests were also conducted.

Through the results of soil physical property experiments and wave settings, the predicted values are calculated and compared with the measured values of the model.

doi:10.6342/NTU202404035

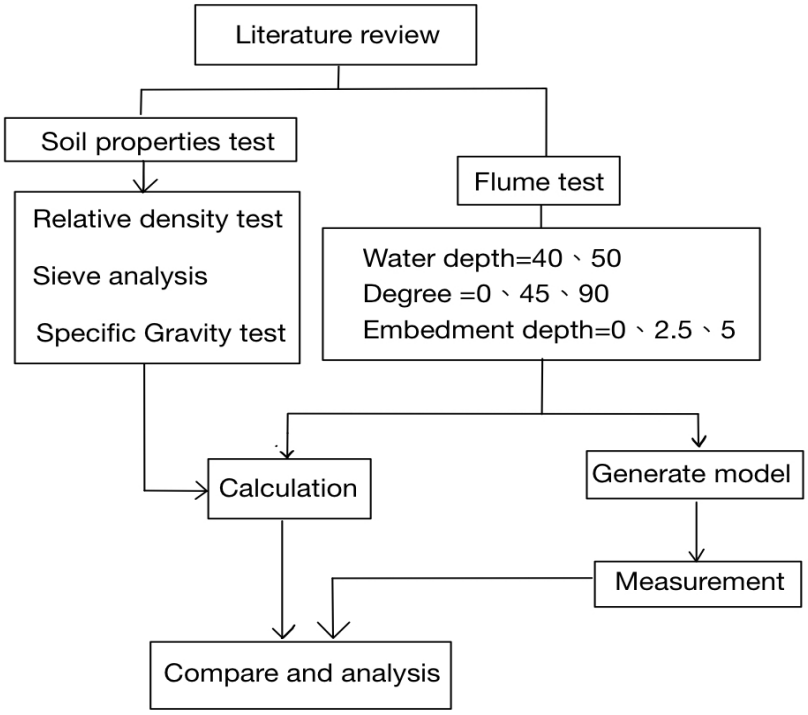

Figure 3.1 Flow chart

3.1 Experimental Set-up

The experiment was conducted in an open flume at the National Taiwan Ocean University. The flume has dimensions of 28 meters in length, 0.8 meters in width, and 0.8 meters in depth. The soil was placed inside a box measuring 0.888 meters in length and 0.708 meters in width, positioned at a depth of 0.368 meters within the flume. The box was submerged in the flume, and electrical cable models were placed inside the box, as

doi:10.6342/NTU202404035

shown in Figure 3.2

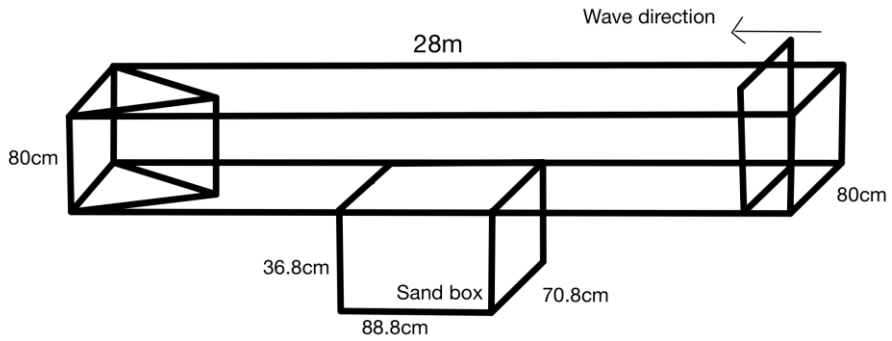

Figure 3.2 Schematic Diagram of flume

Figure 3.3 Wavemaker

For simulating the cable models in this series of experiments, we used PVC pipes with a diameter of 5 centimeters. However, we simplified some conditions.

doi:10.6342/NTU202404035

Regarding the scaling issues in the model, the experiments were conducted under 1g conditions (where g is the acceleration due to gravity). Geotechnical engineers currently debate the stress states of seabed soils. Therefore, we treated the soil as a small-scale prototype model of the seabed.

The experiments involved several variables:

1. The angle of the cable relative to wave direction (0°, 45°, 90°)
2. Cable's embedment depth
3. Water depth.

Figure 3.4 Pipeline perpendicular with wave direction (90 degrees)

doi:10.6342/NTU202404035

Figure 3.5 The pipeline is at 45 degrees to the direction of the wave

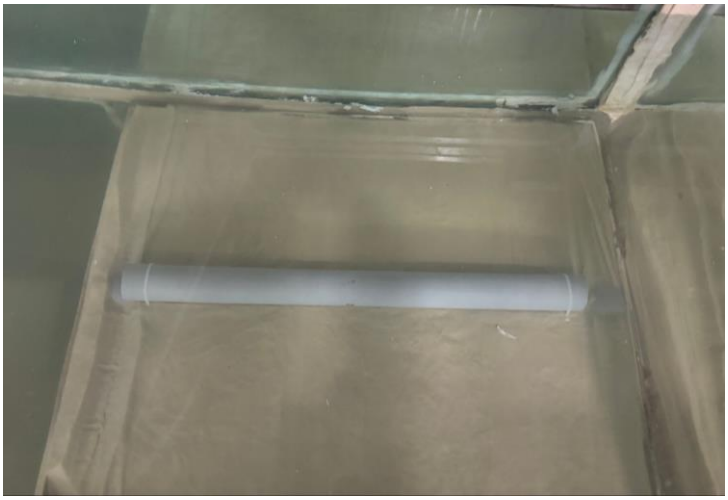

Figure 3.6 Pipeline parallel with wave direction (0 degree)

doi:10.6342/NTU202404035

3.2 Experimental Steps

Before conducting the flume test, preliminary experiments were completed to confirm the properties of the sand. Here are the main steps of the flume experiment:

1. Place saturated sand into the sandbox in the flume
2. Put on the plastic wall, and fill the flume with water
3. Wait for 12 hours for soil consolidation
4. Start the wave maker
5. Add gypsum powder for physical modeling
6. Wait for 2 hours and take off the physical modeling
7. Use Close-range Photogrammetry to generate point clouds.

A plastic wall will be placed before water injection to avoid affecting the soil under the pipe during water injection.

3.3 Experimental Condition

In the flume test, we divided the experiment into two parts: wave conditions and soil conditions.

doi:10.6342/NTU202404035

3.3.1 Wave Condition

Because of the wave generator's limitations, we generated regular waves with a wave height of 10 cm under two water depths, 40 cm, and 50 cm. In addition to cases where pipelines were placed, we also conducted a baseline case with just soil surface, serving as a comparison. The baseline case is that there are no pipes or other structures inside the sandbox, only sand. Table 3-1 shows the wave settings for our experiment.

The numbering rule of the baseline case is baseline case-water depth-wave height. As for the method with pipelines, it is angle-water depth-pipeline burial depth. When there is a pipeline, the wave height is connected to 10 centimeters.

doi:10.6342/NTU202404035

Table 3-1 The setup of the flume test

Teat NO.	h(cm)	H(cm)	f(HZ)	T(s)	D(cm)	e'(cm)
baseline case-50-10	50	10	0.8	1.25	0	
baseline case-40-10	40	10	0.8	1.25	0	
baseline case-50 -7.6	50	7.6	1	1	0	
d0 h50 e2.5	50	10	0.5	2	5	2.5
d0 h40 e0	40	10	0.8	1.25	5	0
d0 h40 e5	40	10	0.8	1.25	5	5
d45 h40 e0	40	10	0.8	1.25	5	0
d45 h50 e5	50	10	0.8	1.25	5	5
d90 h50 e2.5	50	10	0.8	1.25	5	2.5
d90 h40 e2.5	40	10	0.8	1.25	5	2.5
d90 h40 e5	40	10	0.8	1.25	5	5
d90 h40 e0	40	10	0.8	1.25	5	0
d90 h50 e2.5-test	50	10	0.8	1.25	5	2.5

H is the wave height, h is the water depth, e’ is the Pipeline burial depth, and D is the outer diameter of the pipeline.

3.3.2 Soil Condition

In this study, quartz sand was used. Before conducting flume experiments, conduct physical soil testing to determine the basic properties of the soil. In this series of experiments, we set the void ratio of the soil in the sand box to 0.8. Therefore, we added

doi:10.6342/NTU202404035

345 kg of dry sand or 447 kg of saturated sand into a sandbox of approximately 88.8 × 70.8 × 36.8 cm.

Determination of Relative Density

The relative density test was originally supposed to be conducted using ASTM D44253-93 and D4254-91. Considering that the test specimens in this study were mainly composed of fine particles, the limitations of the maximum dry density test instrument may cause a large number of fine particles to scatter and cause test errors. , so we chose to use JSF (T26-81T) for testing. The tools used are depicted in Figure 3.7 (1) two rubber hammers, (2) a 2882.5-gram load block, (3) a mold with an inner diameter of 88.6 mm and inner height of 45.6 mm, (4) a scraper, and (5) a small spoon. The test procedure involves filling the mold with soil sample using a funnel and scraping off excess soil with a scraper positioned inward at the top of the mold to obtain the minimum dry density based on soil volume and weight.

For the maximum dry density of the specimen:

1. Completely dry the soil sample, gently break it apart, and thoroughly mix it. Take approximately 1 kg of the dry soil sample and place it in a drying dish for later use.

doi:10.6342/NTU202404035

2. Layer the dry soil sample into an iron mold equipped with a collar in ten layers. Use a wooden hammer to strike the iron mold horizontally from the outer wall with a 5 cm amplitude for each layer. Rotate the iron mold 45° to 90° after every 5 strikes, totaling 100 strikes.

3. For the first six layers during layering. From the seventh layer onwards, use a collar to prevent the soil sample from escaping the steel mold due to vibration.

4. Remove the collar and quickly scrape the soil sample surface flat with a scraper. Measure the weight of the soil sample inside the steel mold and divide by the volume of the steel mold to obtain the maximum dry density of the soil.

5. Repeat steps (1) to (4) at least three times, exclude any outliers, and select at least three sets of data for average. The average value represents the average maximum dry density of the soil sample.

doi:10.6342/NTU202404035

Table 3-2 The result of JSF(T26-81T)

NO.	Mold weight(g)	Mold + soil weight(g)	soil weight(g)	Volume (cm^3)	γ_{d-max}	$\gamma_{d-max-avg}$
1	1488	1851	363	218.4	1.6620	1.6623
2	1488	1850.4	362.4	218.2	1.6608	
3	1488	1851.9	363.9	218.7	1.6639	
4	1488	1851.8	363.8	218.8	1.6627	

Figure 3.7 The toolset used for the JSF(T26-81T) test

doi:10.6342/NTU202404035

Sieve Analysis

Through Sieve Analysis for soil particle size analysis:

1. Stack the sieves with mesh sizes #10, #40, #60, #100, #140, #170, and #200 in ascending order of mesh size.

2. Pour a certain amount of soil sample into the top sieve.

3. Place the sieves into a sieve shaker and agitate.

4. Weigh the soil retained on each sieve to obtain the results.

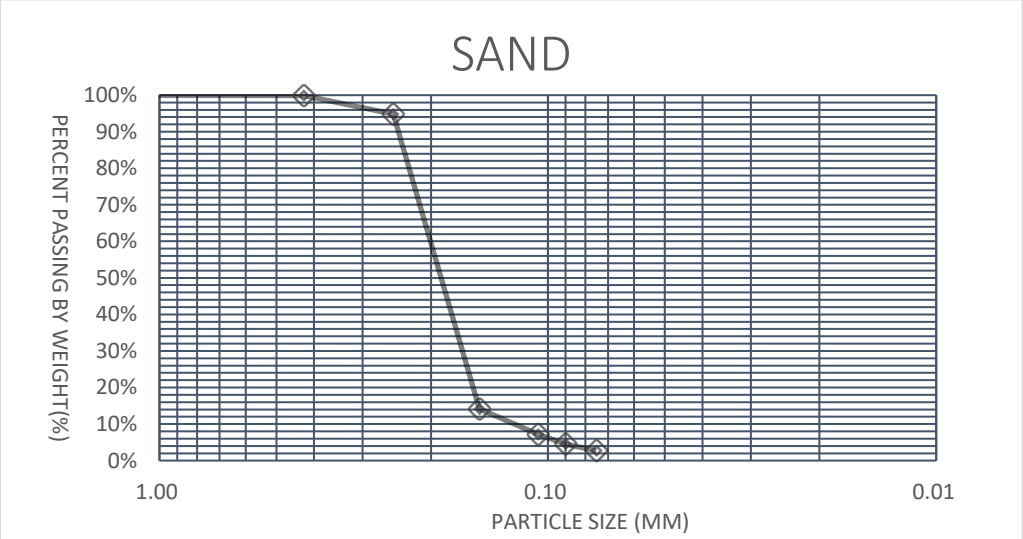

Figure 3.8 particle size analysis

doi:10.6342/NTU202404035

Specific Gravity Test

To determine the Specific Gravity of soil using a pycnometer, follow these steps:

1. Remove the pycnometer from the drying oven and weigh it (m_F).

2. Add approximately dried soil to the pycnometer and weigh it (m_{FS}).

3. Fill the pycnometer with distilled water, ensuring the soil is fully submerged.

4. Place the pycnometer in a water bath with gentle heating, shaking to remove air bubbles. Boil for 15 minutes after reaching boiling point.

5. Allow the pycnometer to cool in a constant temperature water bath until it reaches room temperature. Fill with distilled water up to the mark on the neck of the pycnometer.

6. Wipe off any water from the outside of the pycnometer and weigh it (m_{FSW}).

7. Remove the soil from the pycnometer, wash it thoroughly with distilled water, and then fill it with distilled water again. Place it in a constant temperature water bath until temperature equilibrium is achieved, then fill it with distilled water up to the mark on the neck of the pycnometer.

doi:10.6342/NTU202404035

8. Wipe off any water from the outside of the pycnometer and weigh it (m_{FW}).

9. Calculate Specific Gravity

$$Gs = \frac{ms}{m_S + m_{FW} - m_{FSW}} \quad (3.3.3.1)$$

Table 3-3 Specific gravity test

Test NO.	m_F	m_{FS}	m_{FSW}	m_{FW}	$m_s = m_{FS} - m_F$	$m_s + m_{FW} - m_{FSW}$	Gs	Gs_{avg}
1	69.1	119.14	295.82	264.51	50.04	18.73	2.6716	2.6809
2	80.31	128.75	300.79	270.4	48.44	18.05	2.6836	
3	79.96	112.1	298.5	272.04	42.14	15.68	2.6875	

3.4 Calculation

The following is the calculation process, and the input data comes from wave settings and soil physical property experimental results. The calculation part is divided into two parts, namely scour and sand ripple. To predict the required water particle speed for each, the predicted value is obtained through the previous prediction equation.

doi:10.6342/NTU202404035

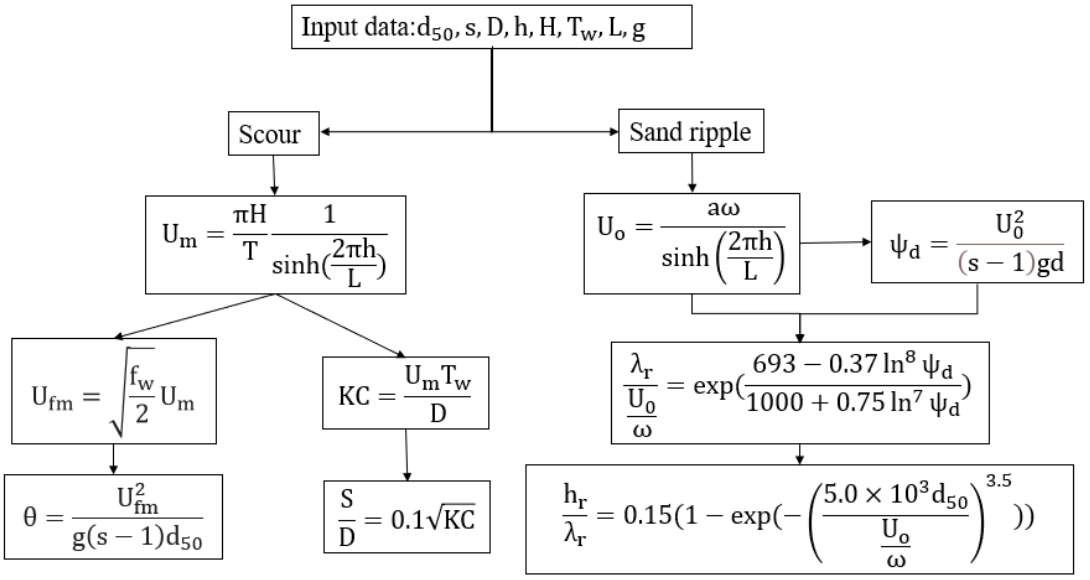

Figure 3.9 Calculation process

where H is wave height, T or Tw is period, h is the water depth, g is the acceleration due to gravity, s is specific gravity of sand, d_{50} is mean particle size of sand, U_m is the maximun value of the orbital velocity at the bed, U_{fm} is the maximun value of the friction velocity, U_o is the amplitude of the oscillations of the horizontal velocity component close to the bottom, ψ_d is sediment mobility number, a is the amplitude of sea wave, ω is angular frequency of the sea waves, θ is the shields parameter, λ_r is the wavelength of sand ripple, h_r is the height of sand ripple.

3.5 Close-range Photogrammetry

Close-range Photogrammetry has been widely used in recent years in civil

doi:10.6342/NTU202404035

engineering. It is a technique that utilizes cameras or other imaging devices to capture images of target objects. By analyzing the feature points in these images, it measures and reconstructs the three-dimensional shape, dimensions, and position of the objects.The availability of video and digital cameras combined with direct access to digital image data has introduced new concepts for close-range applications. Offline photogrammetric systems employ high-resolution digital single-lens reflex cameras, retro-reflective object targets, and sub-pixel image point measurements. They utilize robust bundle adjustment (including self-calibration) to provide object measurements within minutes.

Rick-Zapp et al. (2009) Offline photogrammetry systems provide the highest levels of accuracy and precision. Image point measurement accuracy is up to 1/50 pixel, with typical measurement accuracy (RMS 1-sigma) ranging from 1:100,000 to 1:200,000.

doi:10.6342/NTU202404035

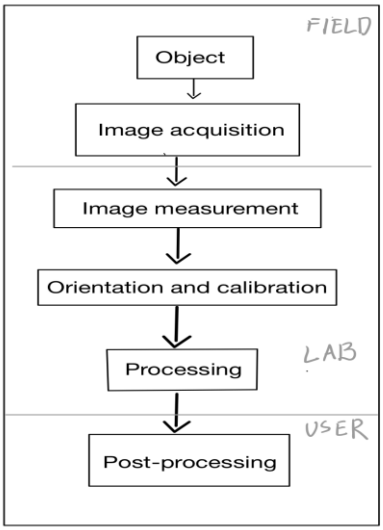

Figure 3.10 Operational stages for offline systems.

Figure 3.10 shows the operational steps of the offline system used in our experiment. In this experiment, we used the built-in camera of an iPhone 13 Pro for capturing images. To ensure the accurate reproduction of real dimensions, a ruler was placed next to the gypsum model during the modeling process, as shown in Figure 3.11

The actual modeling process is as follows:

1. Take photos around the model on site (at different heights and angles)

2. Use Agisoft metashape software for point cloud modeling, but this point cloud model only has the correct geometric shape, but not the actual size, as shown in Figure 3.12

3. When performing analysis, the point cloud is imported into cloud compare. And

doi:10.6342/NTU202404035

adjust the point cloud model to the actual size in cloud compare. As shown in Figure 3.13 to Figure 3.15

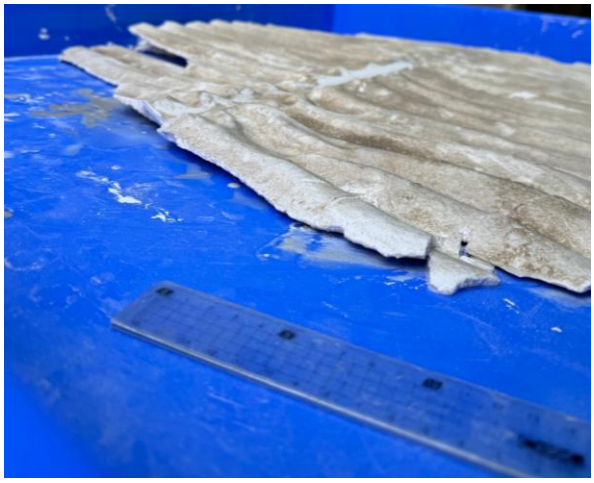

Figure 3.11 Part of plaster statue and ruler

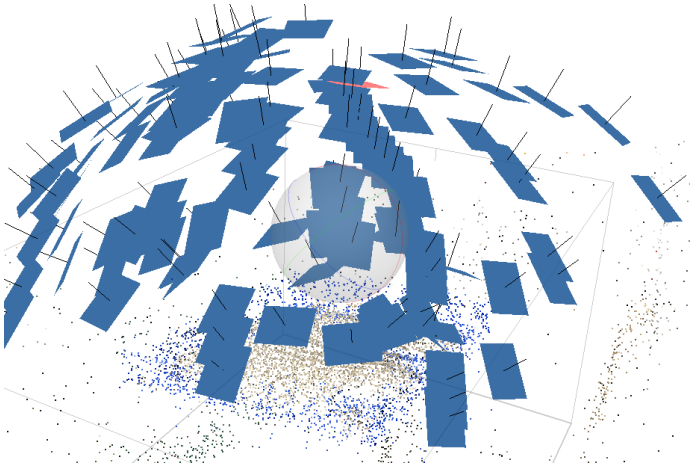

Figure 3.12 Used Agisoft Metashape to make a point cloud model

doi:10.6342/NTU202404035

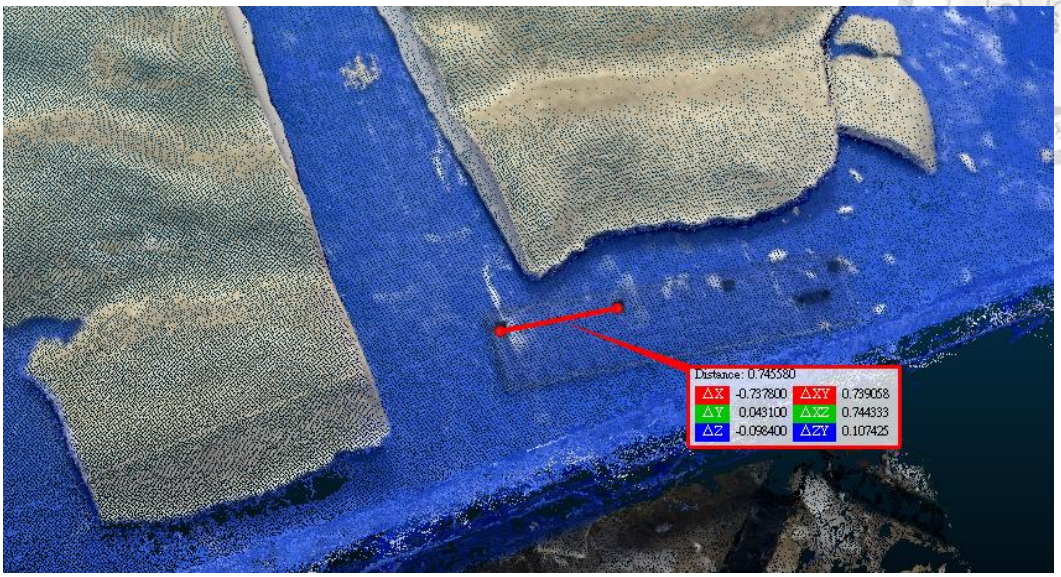

Figure 3.13 Put point cloud into cloud compare

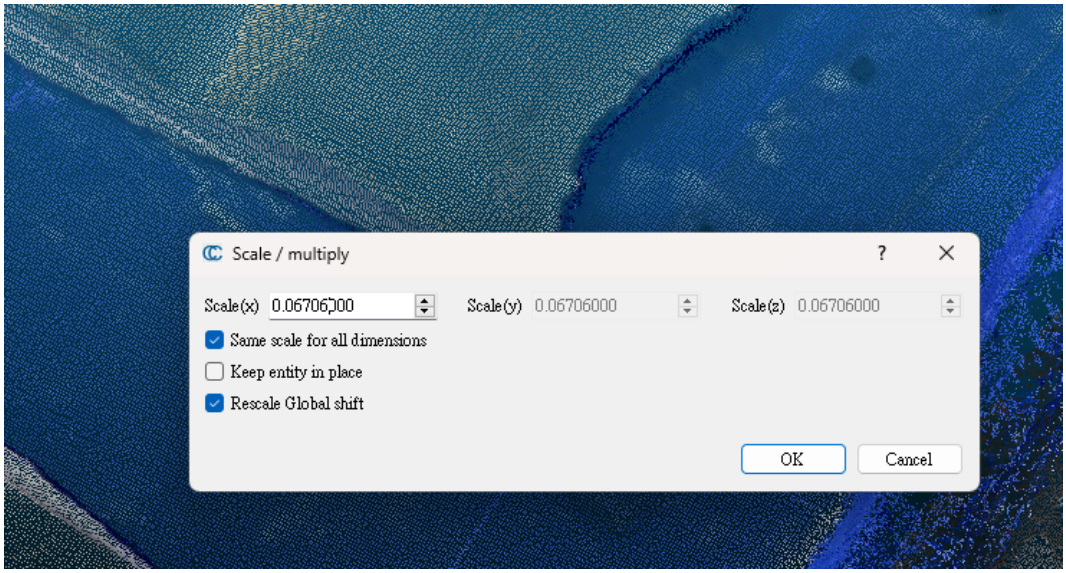

Figure 3.14 Modify the model by cloud compare

doi:10.6342/NTU202404035

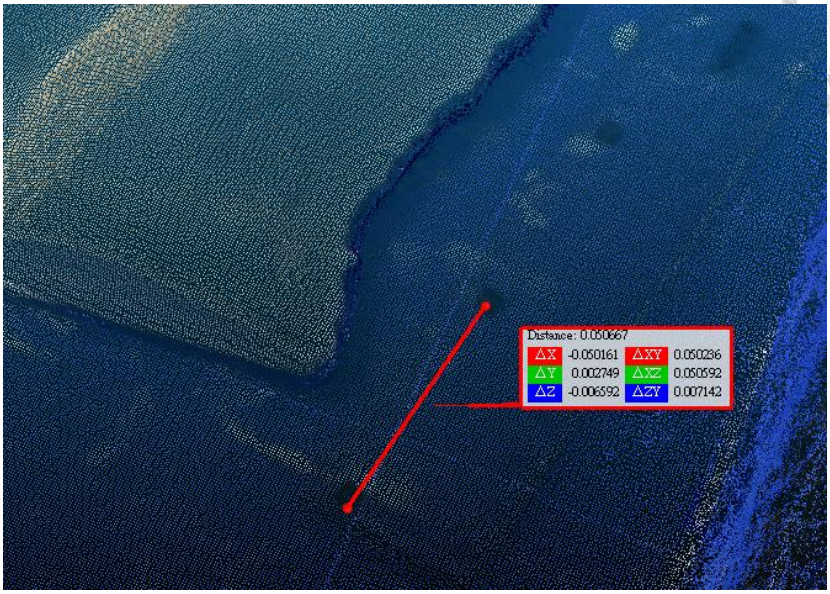

Figure 3.15 Finish

doi:10.6342/NTU202404035

Chapter 4 Results and Discussions

Figure 4.1 to Figure 4.12 are our modeling results through Close-range photogrammetry. The yellow rectangular box houses the pipe. The reason why the plaster cracks is that during the process of removing the plaster, due to the uneven thickness and uneven stress of the plaster, the cracking starts from the thinnest part. It can be found that, except for the baseline case 50-7.6 model, the sand bed surface is very flat and remains in its initial state without any changes. In other cases, the seabed develops shear stresses caused by the movement of water particles near the seabed, causing the surface of the sand bed to become uneven. In this chapter, we analyze scour conditions, sand bed surface characteristics, and compare them with equations predicted by previous studies.

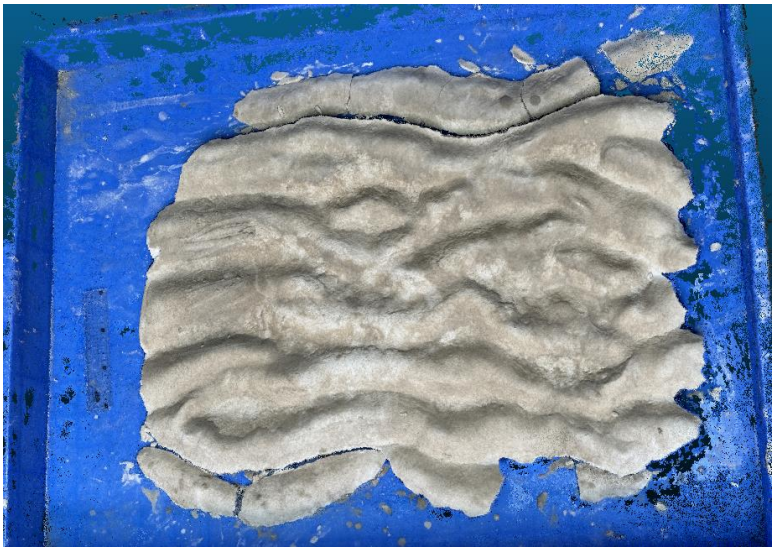

Figure 4.1 The result of baseline case-50-10

doi:10.6342/NTU202404035

Figure 4.2 The result of baseline case-40 -10

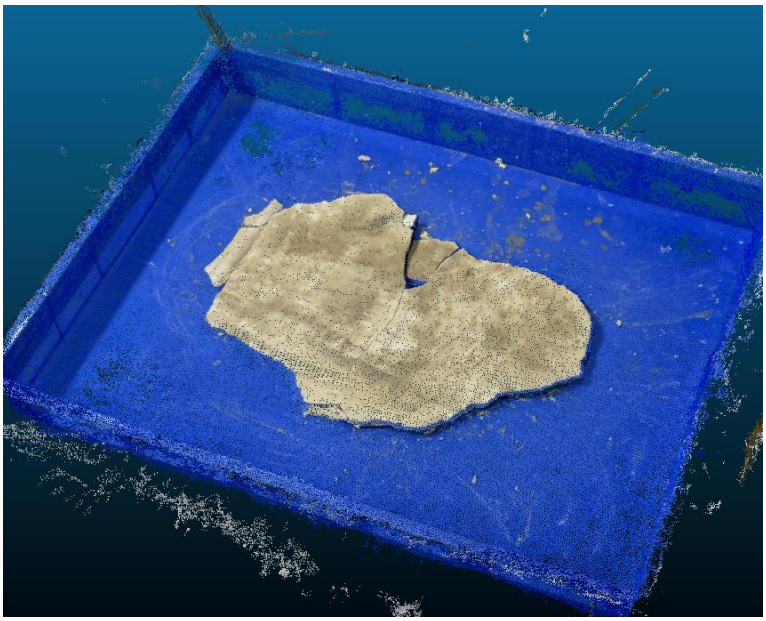

Figure 4.3 The result of baseline case-50 -7.6

doi:10.6342/NTU202404035

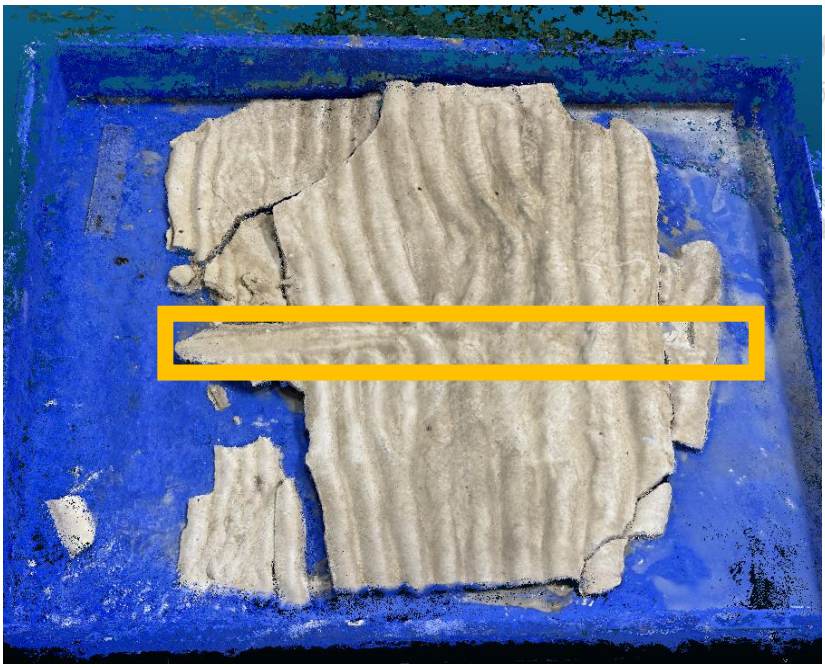

Figure 4.4The result of d0 h40 e0

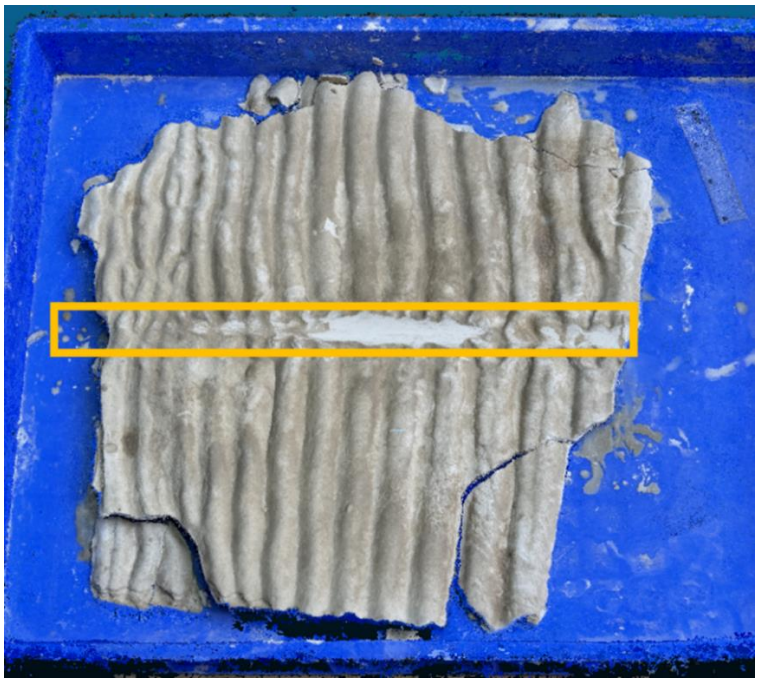

Figure 4.5 The result of d0 h40 e5

doi:10.6342/NTU202404035

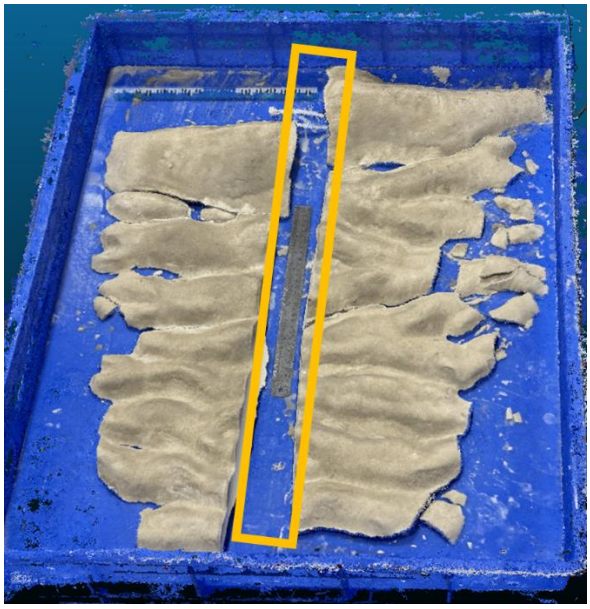

Figure 4.6 The result of d0 h50 e2.5

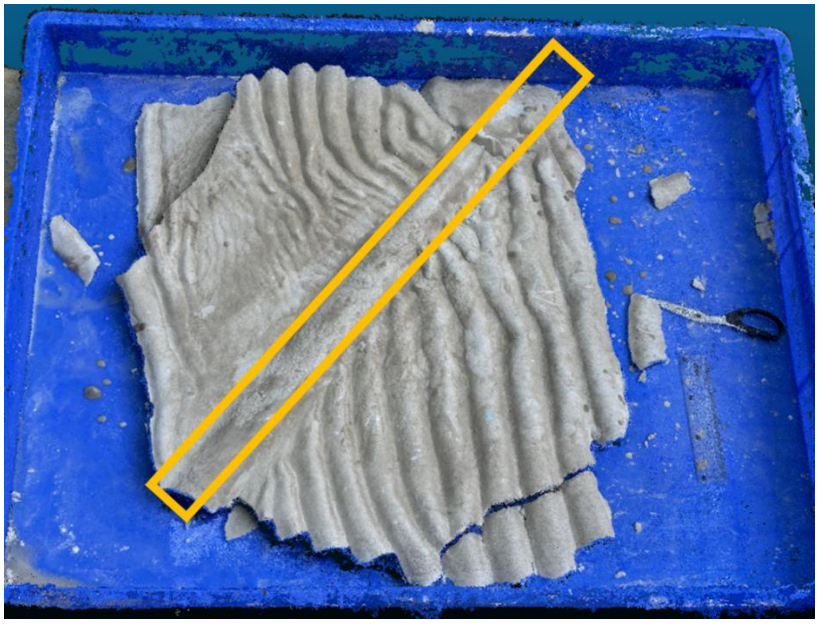

Figure 4.7 The result of d45 h40 e0

doi:10.6342/NTU202404035

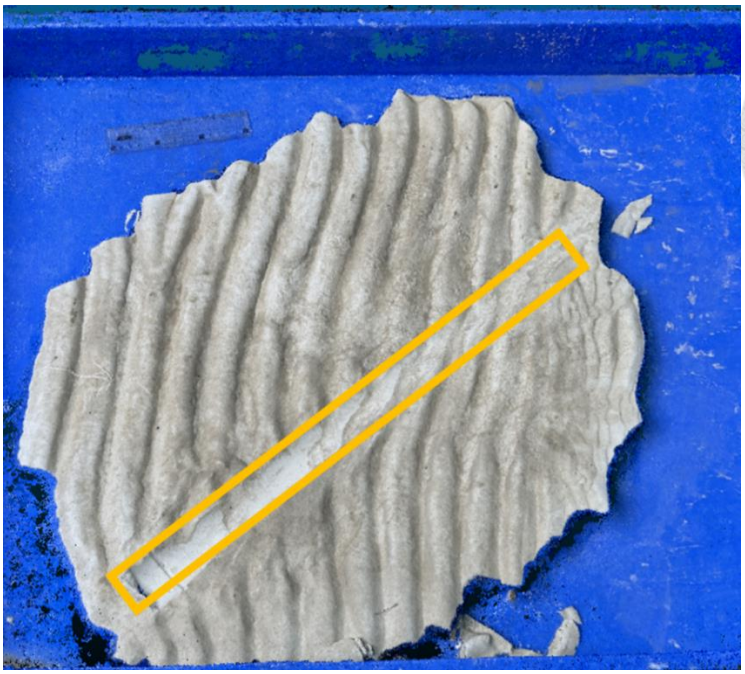

Figure 4.8 The result of d45 h40 e5

Figure 4.9 The result of d90 h50 e2.5

doi:10.6342/NTU202404035

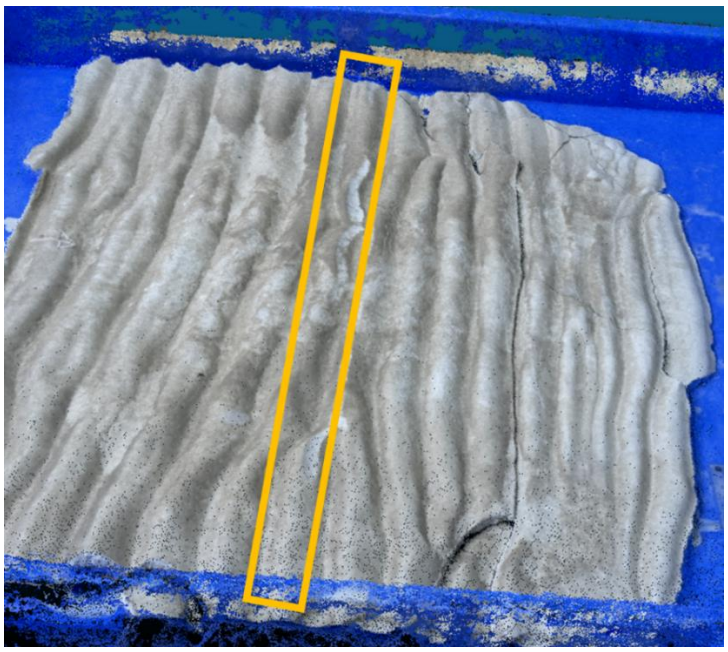

Figure 4.10 The result of d90 h40 e5

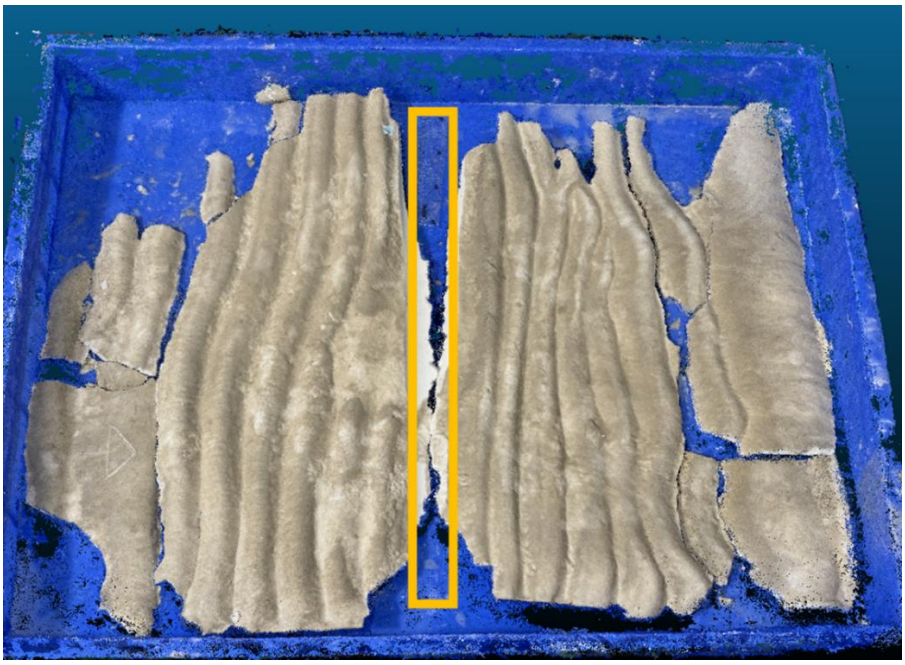

Figure 4.11 The result of d90 h40 e2.5

doi:10.6342/NTU202404035

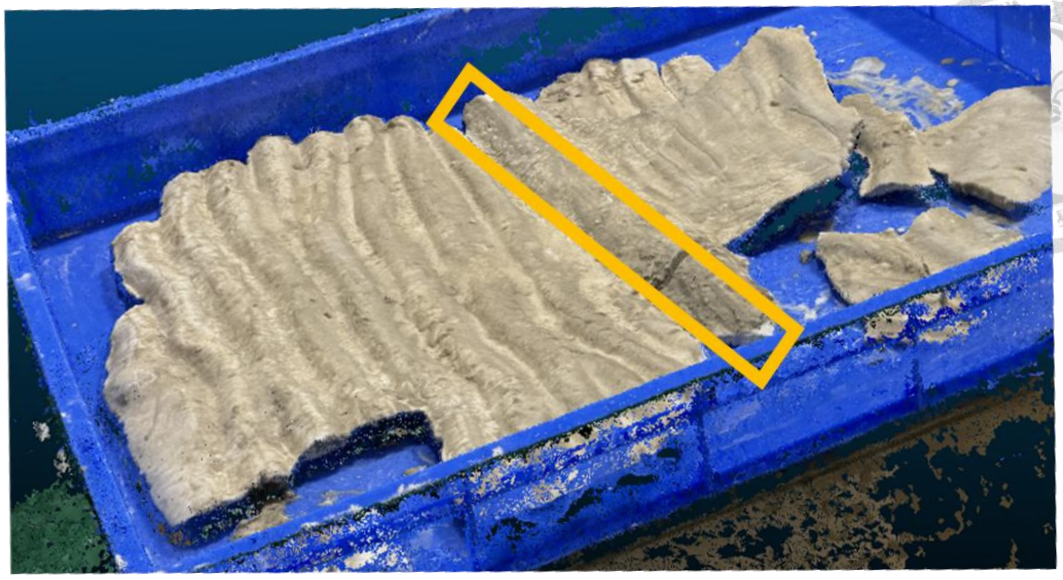

Figure 4.12 The result of d90 h40 e0

Figure 4.12 The result of d90 h50 e2.5-test

doi:10.6342/NTU202404035

4.1 Criterion of Scour

Table 4-1 is the bed friction velocity and θ calculated according to the set experimental conditions. The coefficients in Table are calculated based on the formula of (2.3)(2.4)(2.5)(2.6). Sumer et al. (2001) believe that Scour will occur when $\theta > \theta_{cr}$. In our experiments, θ is smaller than $\theta_{cr}(\theta_{cr} \approx 0.048)$. But in the three cases of d90 h40 e0, d45 h40 e 0, and d90 h40 e2.5-test, we can find the occurrence of scour from the plaster statues, as shown in Figure 4.13 to Figure 4.15. The part with the red line is where we think scour occurs.

The reason we speculate is that the water particle speed in our experiment is different from the theoretical value. According to Chen (2010), when the water tank creates waves, the difference between the water particle speed and the theoretical value is about 10%. Table 4-2 considers a 10% water particle velocity difference, and then calculates other correlation coefficients. It can be seen that after increasing the water particle velocity by 10%, the case with a water depth of 40 cm is already very close to the critical shields parameter.

doi:10.6342/NTU202404035

Table 4-1 Theoretical experimental conditions

Teat NO.	U_m(cm/s)	KC	α	U_{fm}	θ
baseline case-50-10	18.026	/	3.586	1.922	0.027
baseline case-40-10	20.974	/	4.173	2.195	0.035
baseline case-50 -7.6	12.283	/	1.955	1.413	0.014
d0 h50 e2.5	18.026	4.506	3.586	1.922	0.027
d0 h40 e0	20.974	5.243	4.173	2.195	0.035
d0 h40 e5	20.974	5.243	4.173	2.195	0.035
d45 h40 e0	20.974	5.243	4.173	2.195	0.035
d45 h50 e5	18.026	4.506	3.586	1.922	0.027
d90 h50 e2.5	18.026	4.506	3.586	1.922	0.027
d90 h40 e2.5	20.974	5.243	4.173	2.195	0.035
d90 h40 e5	20.974	5.243	4.173	2.195	0.035
d90 h40 e0	20.974	5.243	4.173	2.195	0.035
d90 h50 e2.5-test	18.026	4.506	3.586	1.922	0.027

Table 4-2 10% correlation coefficient for water particle velocity difference

h(cm)	H(cm)	U_m(cm/s)	KC	α	U_{mf}	θ
50	10	19.83	4.9575	3.945	2.090	0.032
40	10	23.07	5.7675	4.590	2.386	0.041

doi:10.6342/NTU202404035

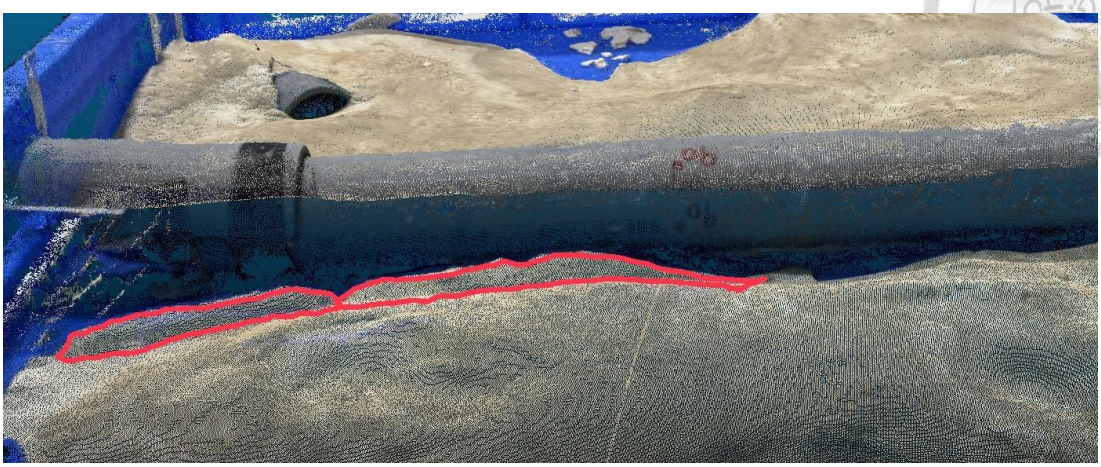

Figure 4.13 Scour found in d90 h40 e2.5-test

Figure 4.14 Scour found in d90 h40 e0

doi:10.6342/NTU202404035

Figure 4.15 Scour found in d45 h40 e0

4.2 Analysis between d90 h50 e2.5-test and d90 h50 e2.5

For d90 h40 e2.5-test and d90 h40 e2.5 under the same wave conditions, we could not find the same situation in the plaster mold of d90 h50 e2.5, so we analyzed the possible reasons.

In the two experiments, the methods of making the sand bed are different. When making the d90 h40 e2.5-test, the steps are as follows:

1. Fill the water tank to a depth of 50cm

2. Submerge the sandbox into the water and place it at the designated location

doi:10.6342/NTU202404035

3. Surround the sandbox with a homemade plastic wall

4. Start pouring sand into the sandbox

5. Confirm with your hands whether the surface of the sand bed is flat

However, this production method caused some problems. After standing for a day, the water became turbid like miso soup as shown in Figure 4.16, and it was impossible to confirm the sand bed with the naked eye. At the same time, there is no guarantee that all the sand particles will enter the sandbox. Some of the sand will fall outside the sandbox, causing the sand in the sandbox to not reach the expected weight, because the sand in the sandbox will be less than we expected. The porosity is even greater. Therefore, we switched to the method described in Chapter 3, and the problem of invisible soil surface was indeed solved.

Therefore, we believe that the reason why d90 h40 e2.5-test will produce Scour is that the sand bed we made is looser than that of d90 h40 e2.5, so the two have different phenomena.

doi:10.6342/NTU202404035

Figure 4.16 Water-like miso soup

4.3 Scour Depth

According to (2.8) (2.17)(2.18), we can see that the predicted scour depth and width are slightly different from the actual value, as shown in Table 4-3.

Table 4-3 Sour predicted depth versus actual depth

Test NO.	Predictive depth (m)	actual depth (m)	Predictive width (m)	actual width (m)
d45 h40 e0	0.0083786	0.010383	0.1198364	0.0665
d90 h40 e0	0.0114455	0.015106	0.1706366	0.088311

It may be caused by the following reasons:

1. U_m is different from the theoretical value

2. The sand box is not completely flush with the bottom of the sink, which affects the movement of water particles at the bottom.

doi:10.6342/NTU202404035

3. (2.9) is an empirical formula

Figure 4.18 is based on the comparison between the collected wave-induce scour depth and (2.8).Because the scour depths are 0.010383 m and 0.015106, no scour can be observed in the cases with burial depths of 0.05m and 0.025m.

Similar to the study by Zang et al. (2019), when the angle increases from 0 degrees to 45 degrees, the scour depth S/S0 changes from 1 to about 0.7, and the experimental data we obtained this time are compared with previous experimental data, basically overlap.

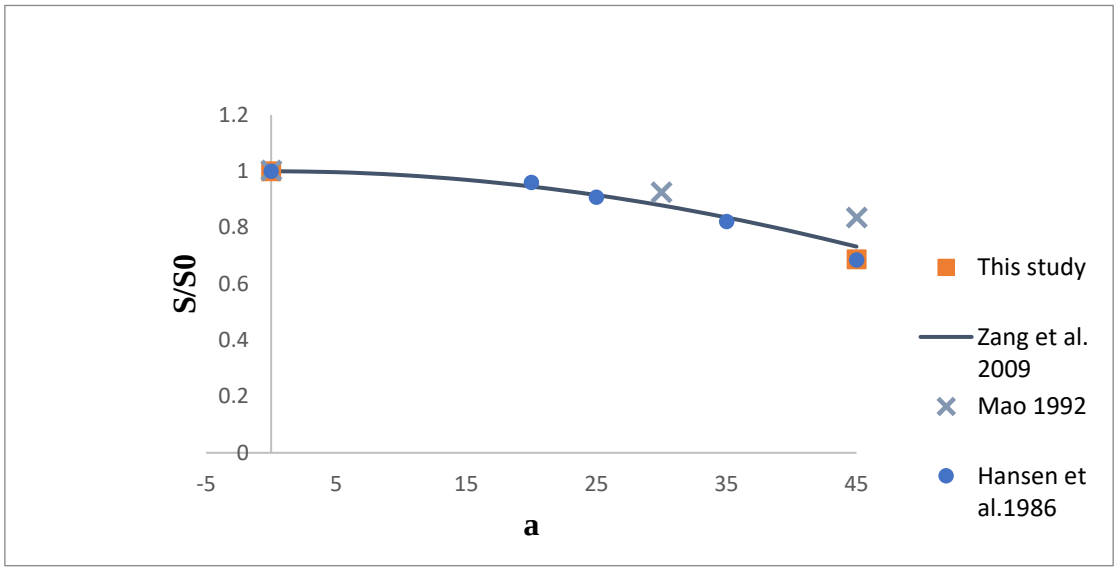

Figure 4.17 Scour depth ratio verse pipeline angle

doi:10.6342/NTU202404035

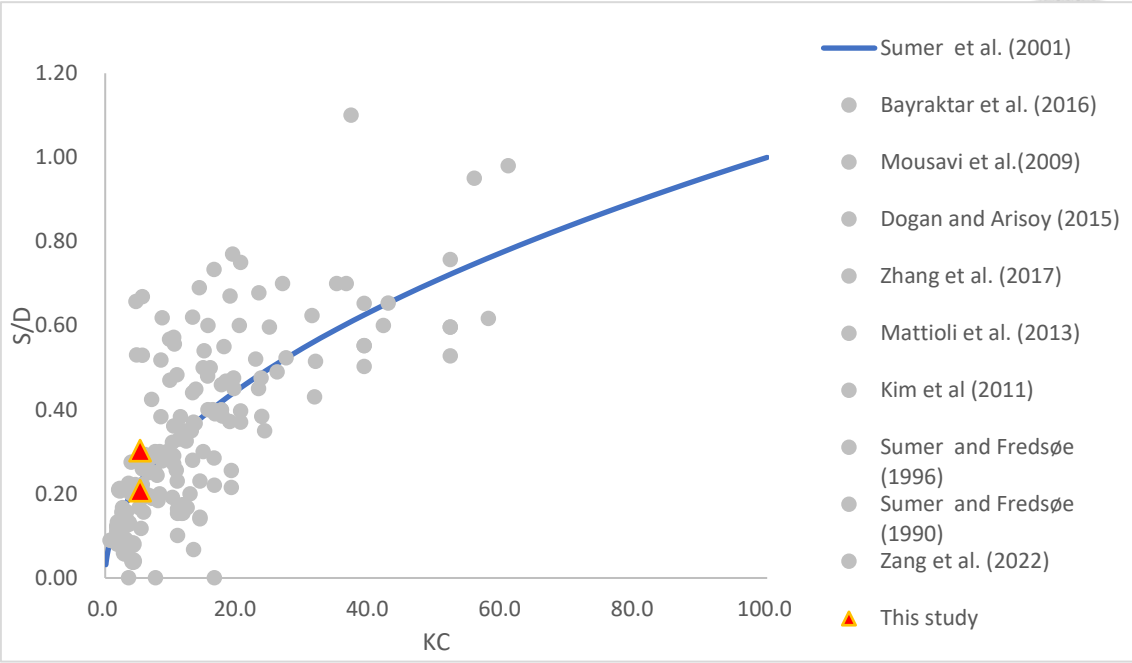

Figure 4.18 Data of wave-induce scour depth

4.4 Sand Ripple Height and Wavelength

We believe that the movement of water particles is caused by the sandbox. The protruding part of the sandbox causes Lee wake, which in turn causes Lee erosion and sand ripple.

To compare with the prediction formulas proposed by previous people, Table 4-4 is calculated based on (2.31)(2.32)(2.33) and the data we obtained using Cloud Compare .

Figure 4.20 to Figure 4.41 are the captured data points. In the part of sand ripple height, we take the adjacent peaks and troughs as data points. It should be noted that in the part of sand ripple height, we use ΔZ as a data point, the sand ripple wavelength uses the Distance between two points. Each model is averaged to obtain sand ripple height and

doi:10.6342/NTU202404035

sand ripple wavelength.

We can find that there are three cases in Table 4-4: baseline case-50-10, d0 h50 e2.5, d90 h50 e2.5, the wave height is larger than the predicted value and the wavelength is larger than the predicted value, and the rest are smaller than the predicted value, so it cannot be completely consistent. Compared with the data collected by Nelson et al. (2013), it is still within a reasonable range.

In terms of sand ripple height, when only the water depth changes, our experimental data tends to be different from the theoretical value. We can find that as the water depth increases, the sand ripple height decreases, and our experiment data. As the water depth increases, the sand ripple height increase.

We speculate that in the prediction formula, the water depth of 40 cm and 50 cm falls within the agreed value range, which is the error range. This may also be why there is a difference between the measured value and the predicted value.

doi:10.6342/NTU202404035

Table 4-4 Sand ripple wavelenght and height

Teat NO.	U_o/ω	ψ_d	λ r-Prediction	hr-Prediction	hr/λr-Prediction	λr--Measurement	hr-Measurement	hr/λr-Measurement	different of wavelenght	different of height
baseline case-50-10	2.57	1.2	4.71	0.71	0.15	7.15	0.83	0.12	51.86%	17.59%
baseline case-40-10	3.48	2.2	6.08	0.91	0.15	4.49	0.43	0.1	-26.12%	-52.88%
baseline case-50 -7.6	1.01	0.3	1.98	0.3	0.15	0	0	/	/	/
d0 h50 e2.5	3.59	0.9	6.69	1	0.15	7.63	2.09	0.27	14.18%	108.04%
d0 h40 e0	3.48	2.2	6.08	0.91	0.15	3.84	0.32	0.08	-36.90%	-64.72%
d0 h40 e5	3.48	2.2	6.08	0.91	0.15	4.46	0.47	0.11	-26.65%	-48.46%
d45 h40 e0	3.48	2.2	6.08	0.91	0.15	3.77	0.49	0.13	-38.01%	-46.52%
d45 h50 e5	2.57	1.2	4.71	0.71	0.15	4.33	0.34	0.08	-8.10%	-51.67%
d90 h50 e2.5	2.57	1.2	4.71	0.71	0.15	6.85	1.39	0.2	45.40%	96.39%
d90 h40 e2.5	3.48	2.2	6.08	0.91	0.15	4.37	0.4	0.09	-28.22%	-56.32%
d90 h40 e5	3.48	2.2	6.08	0.91	0.15	4.54	0.56	0.12	-25.36%	-39.03%
d90 h40 e0	3.48	2.2	6.08	0.91	0.15	4.68	0.4	0.09	-23.01%	-55.99%

doi:10.6342/NTU202404035

4.5 Impact of pipelines on sand ripple

(2.31) (2.32) (2.33) designed by previous researchers, the existence of pipelines does not affect the sand ripple height and wavelength. However, in our experiments, it was observed that the existence of pipelines affects the sand ripple height, such as in d45 h40 e0. Diffraction is generated by the gap between the sandbox and the flume wall when the wave passes through the pipe.

In our experiment, when the wave direction is parallel to the wave direction and the pipeline burial depth is 2.5cm, the height of the sand ripples before and after the pipeline does not change much. We don't see any effect of 0 degree piping on sand pattern. When the pipeline is buried to a depth of 5 cm, that is, when the pipeline is completely buried, there is almost no impact on the waves passing through the pipeline, as shown in Figure 4.19. We speculate that the amplitude of water particles is between 2.5 cm and 5 cm, so when the height of the pipe reaches 5 cm, the pipe will hinder the movement of water particles. It is worth noting that in d90 h50 e2.5, an interesting phenomenon was observed. A sand trap larger than the ripples of sand formed behind the pipe.

doi:10.6342/NTU202404035

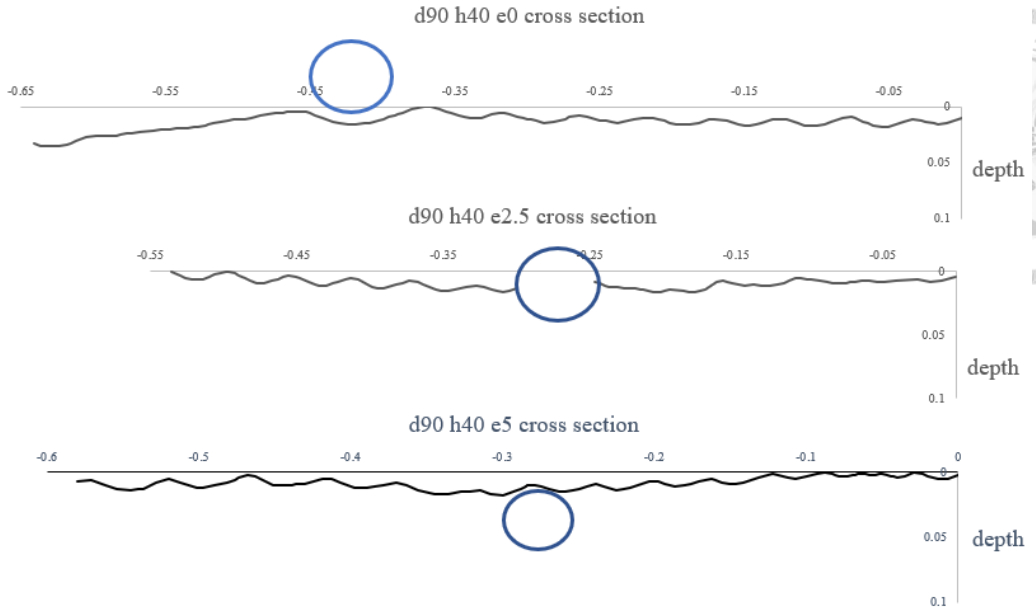

Figure 4.19 Cross section of d90 h40

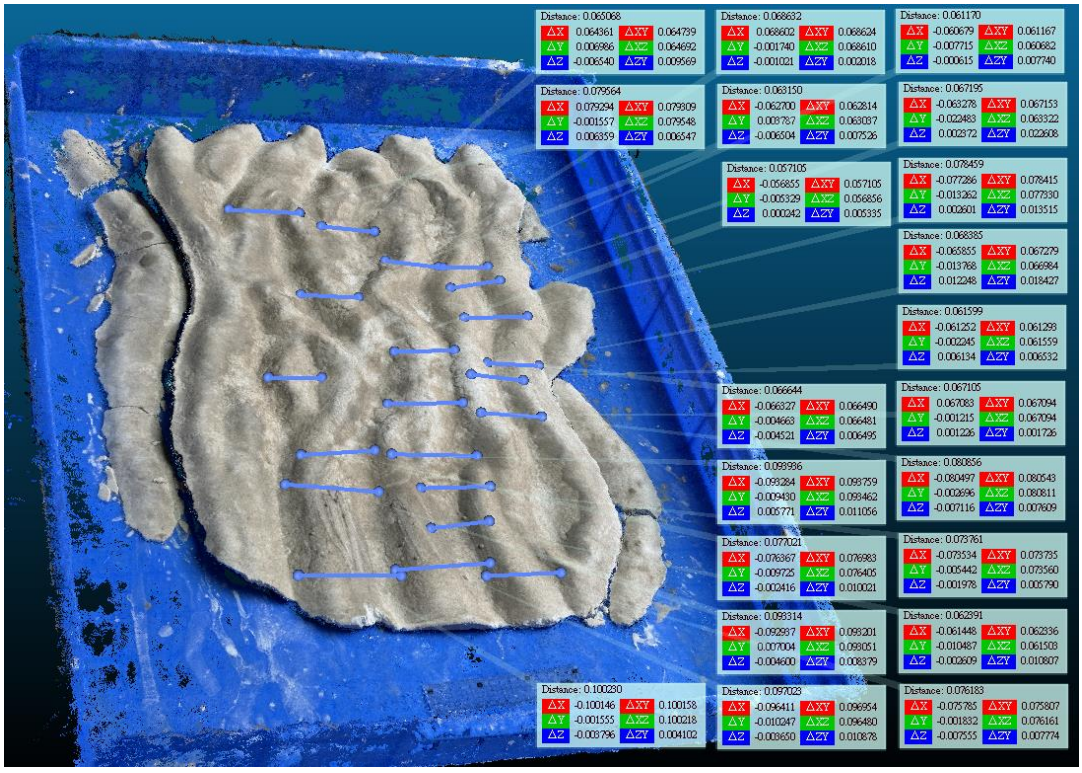

Figure 4.20 Wavelength data points of baseline case-50-10

doi:10.6342/NTU202404035

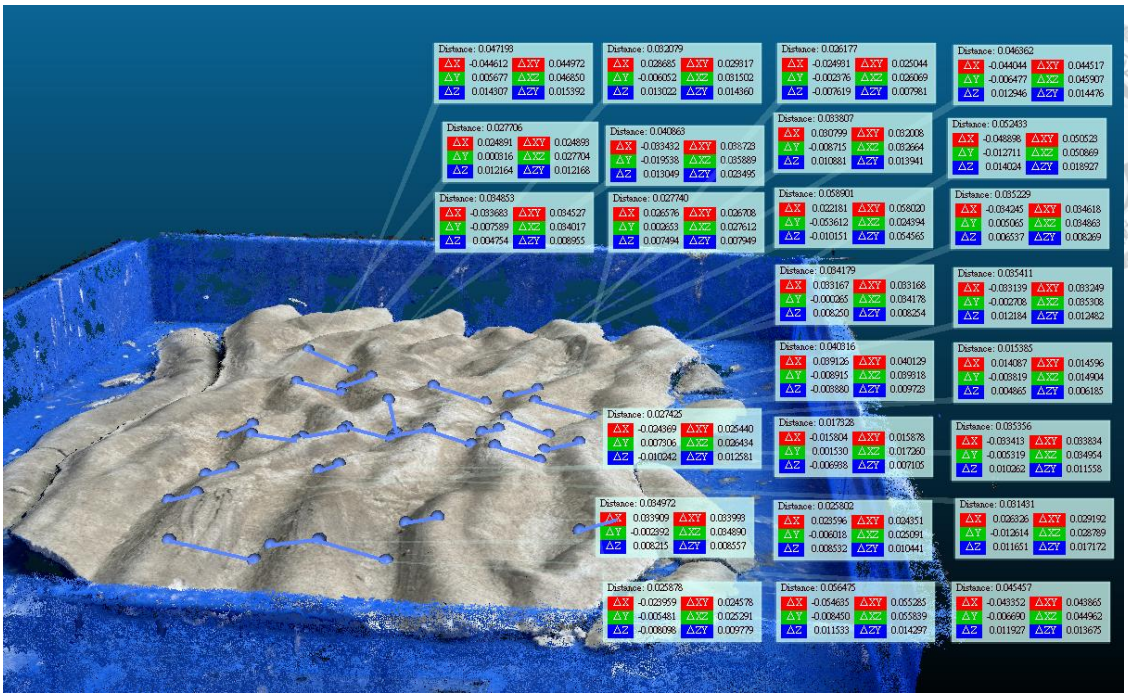

Figure 4.21 sand ripple height data points of baseline case-50-10

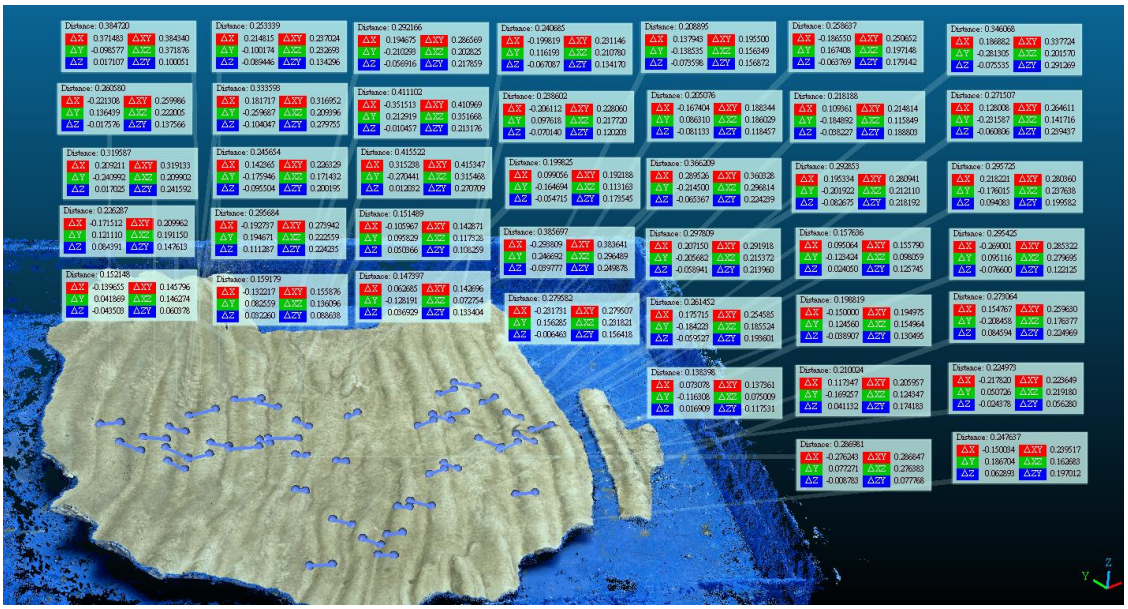

Figure 4.22 Sand ripple height data points of Baseline case-40-10

doi:10.6342/NTU202404035

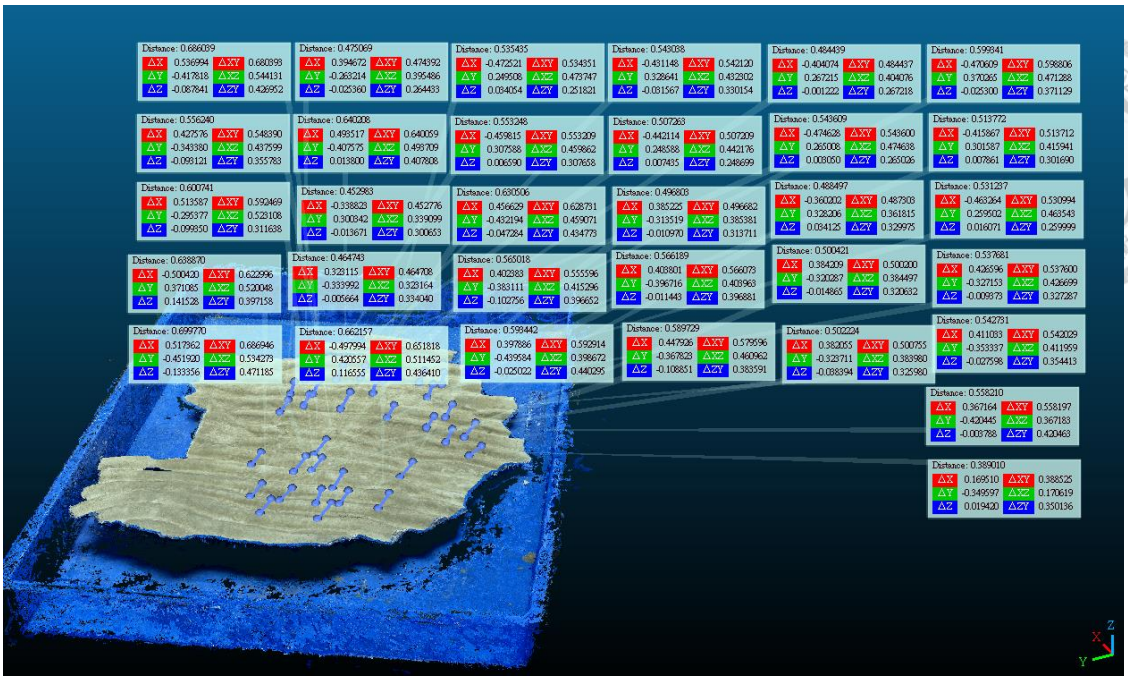

Figure 4.23 Wavelength data points of baseline case-40-10

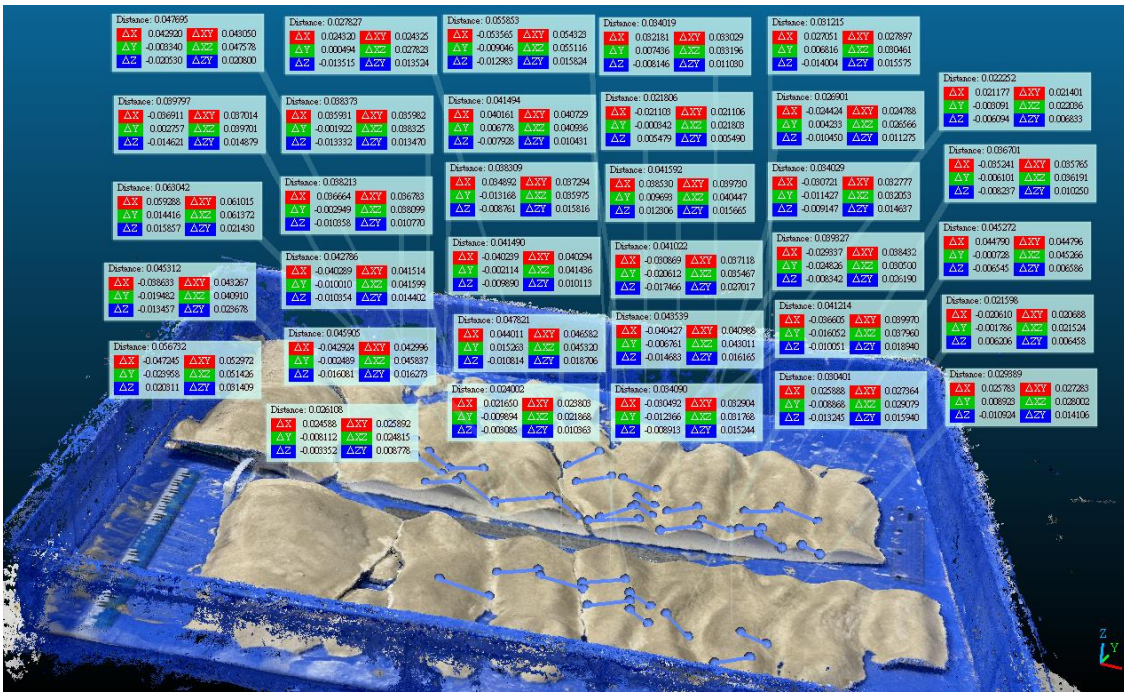

Figure 4.24 Sand ripple height data points of d0 h50 e2.5

doi:10.6342/NTU202404035

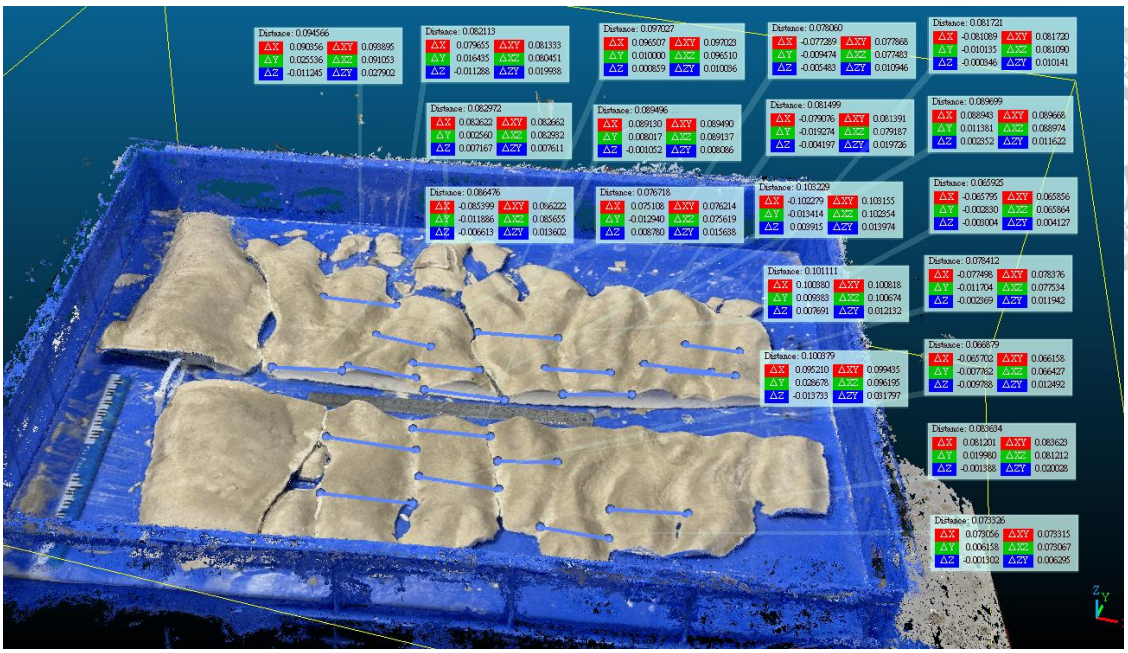

Figure 4.25 Wavelength data points of d0 h50 e2.5

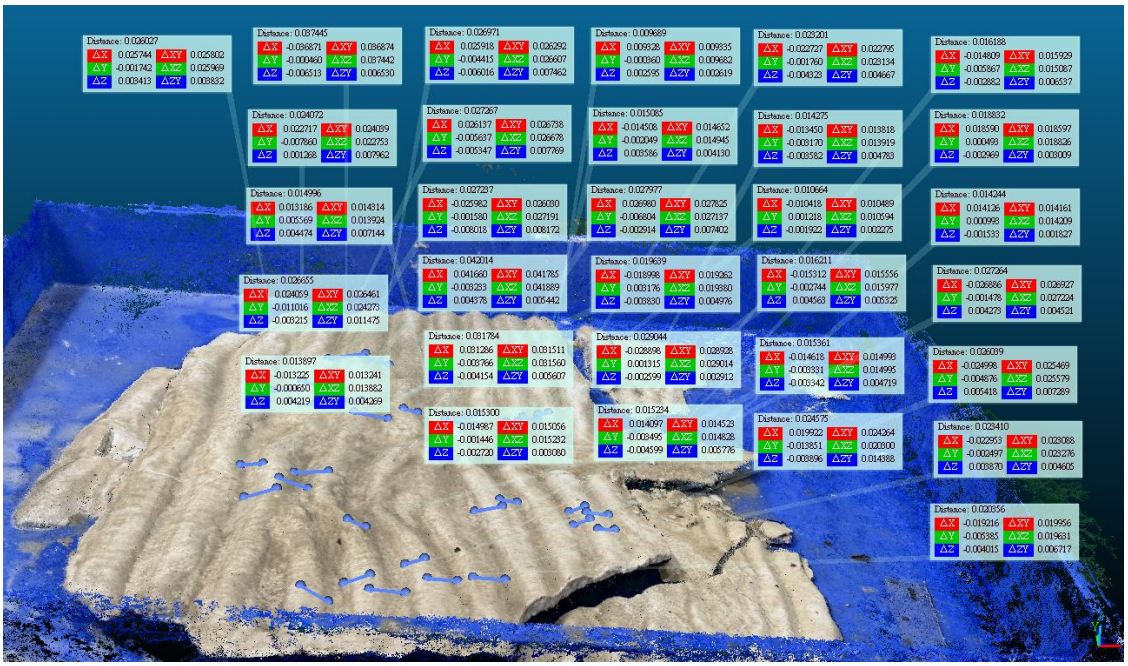

Figure 4.26 Sand ripple height data points of d0 h40 e0

doi:10.6342/NTU202404035

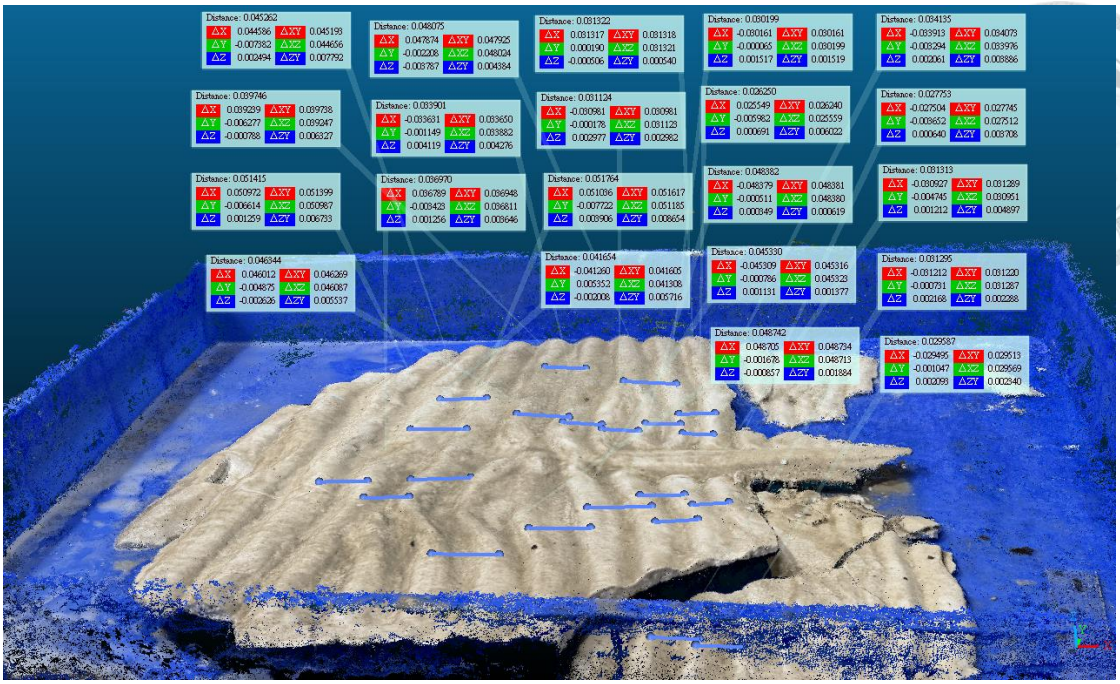

Figure 4.27 Wavelength data points of d0 h40 e0

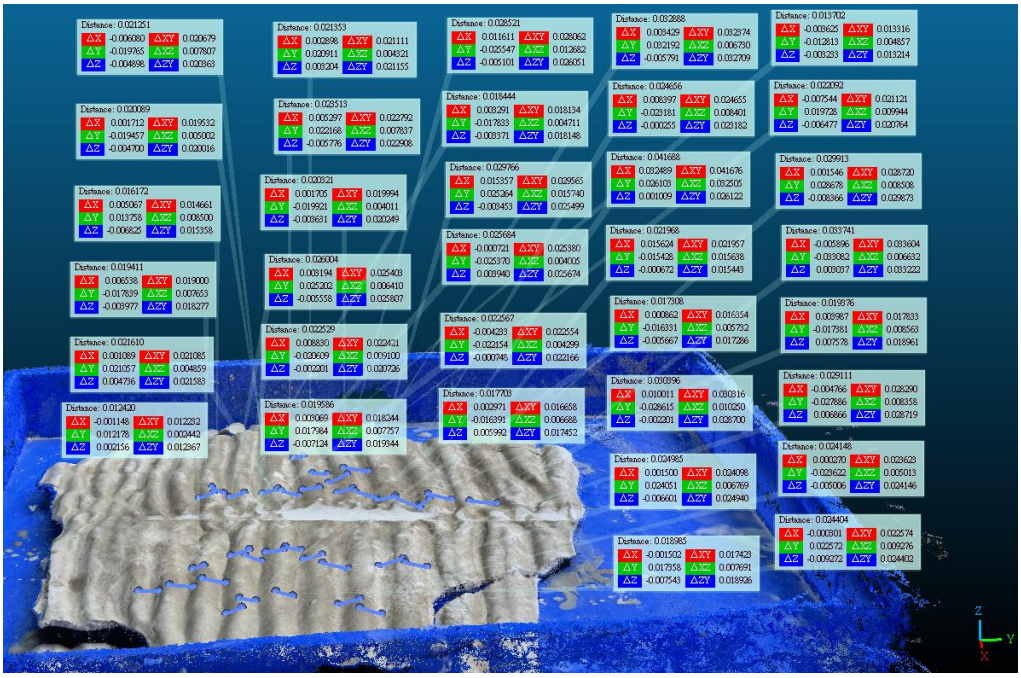

Figure 4.28 Sand ripple height data points of d0 h40 e5

doi:10.6342/NTU202404035

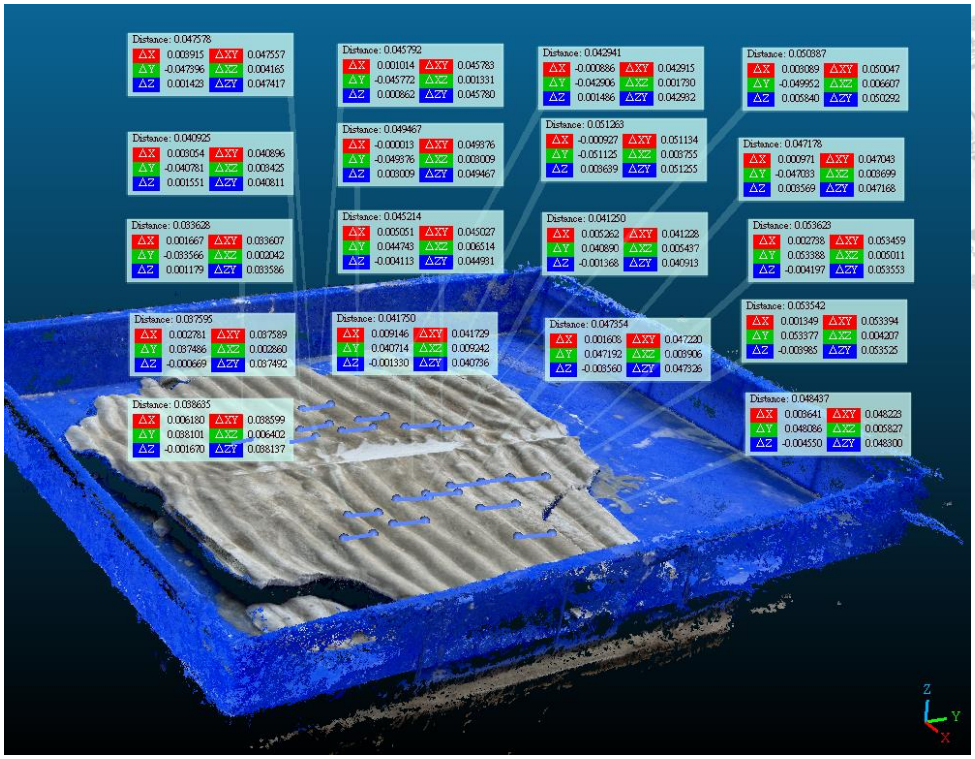

Figure 4.29 Wavelength data points of d0 h40 e5

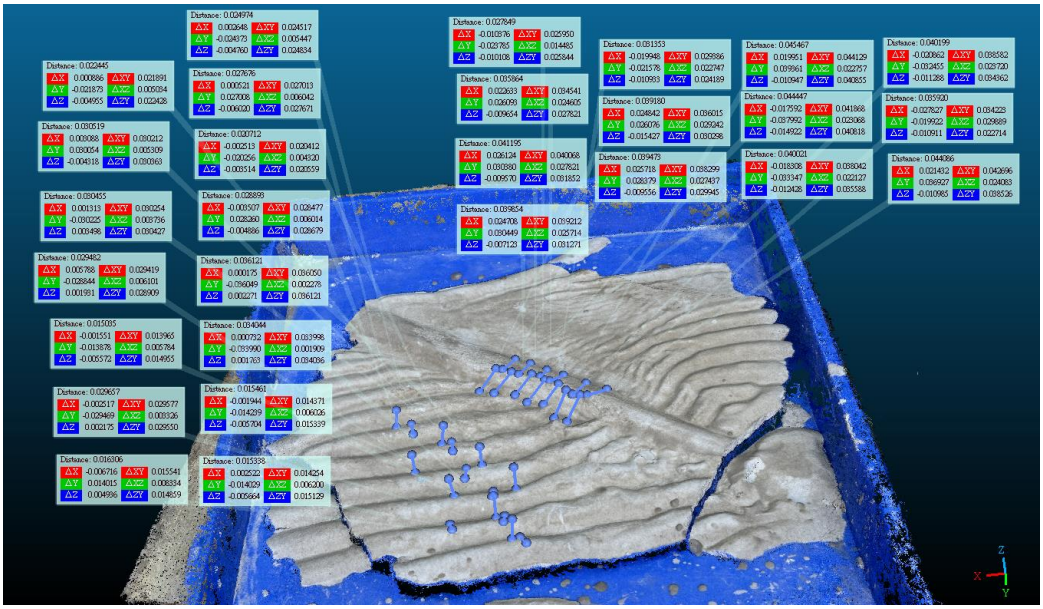

Figure 4.30 Sand ripple height data points of d45 h40 e0

doi:10.6342/NTU202404035

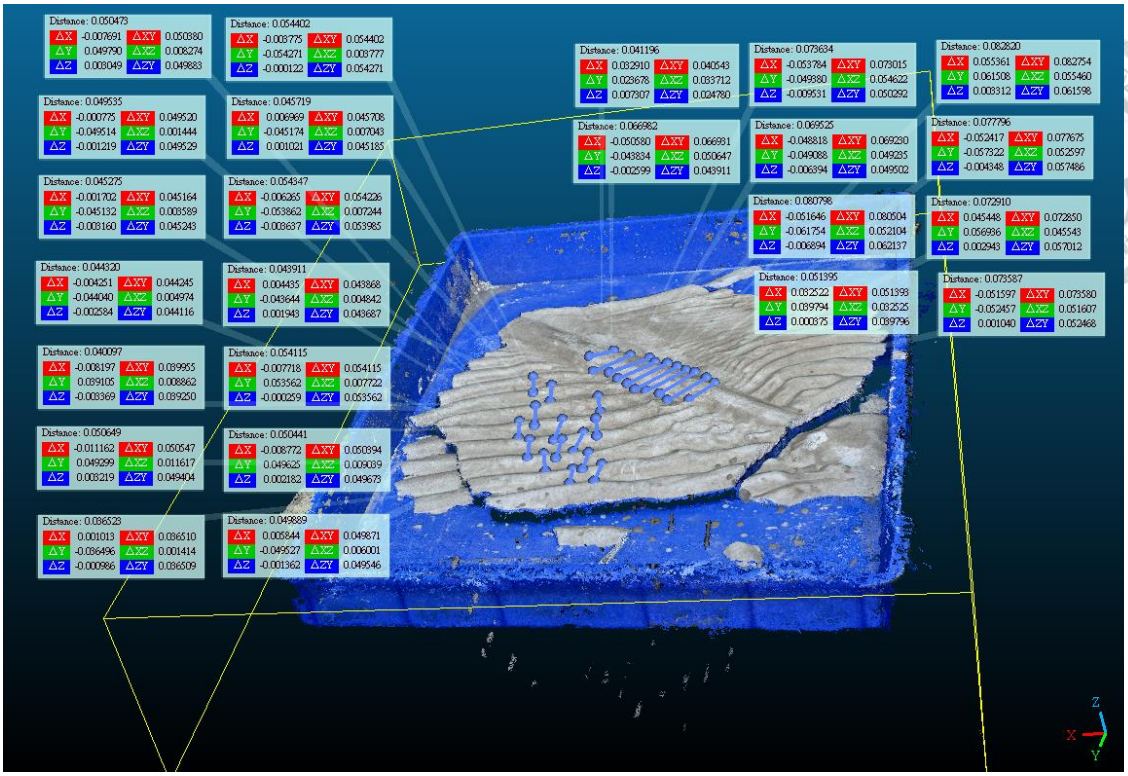

Figure 4.31 Wavelength and scour width data points of d45 h40 e0

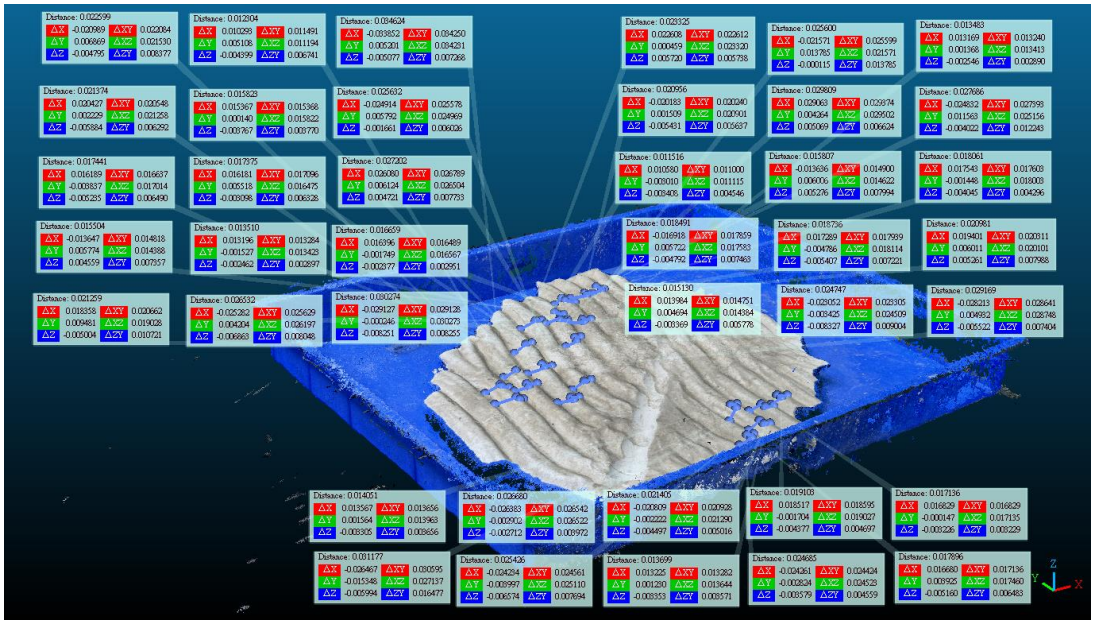

Figure 4.32 Sand ripple height data points of d45 h40 e5

doi:10.6342/NTU202404035

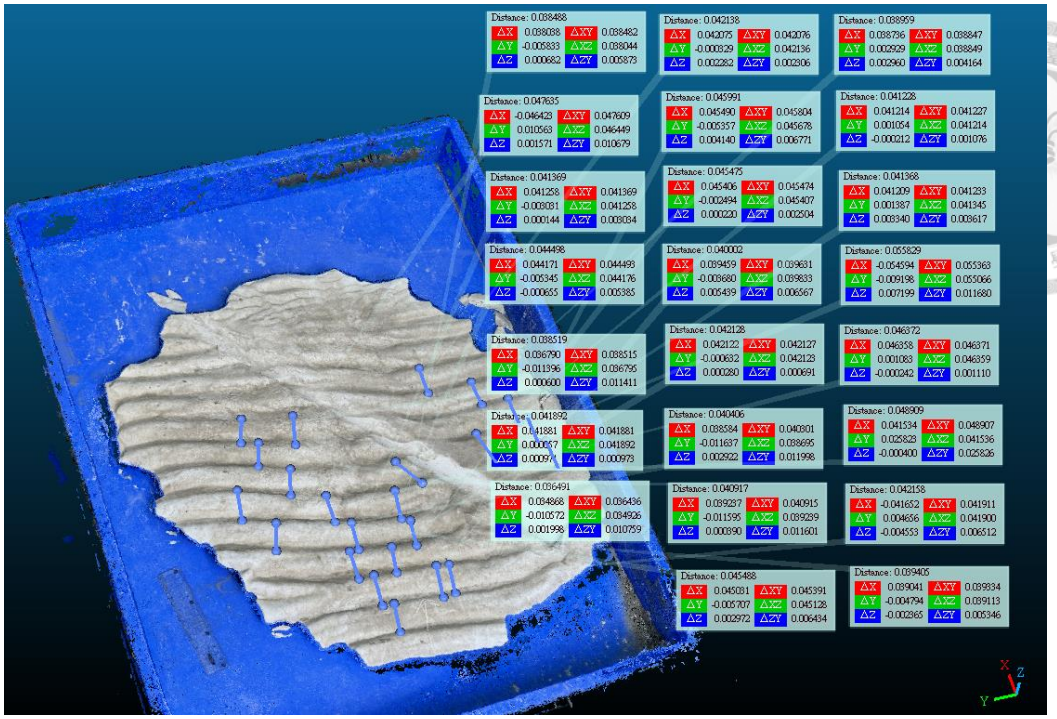

Figure 4.33 Wavelength data points of d45 h40 e5

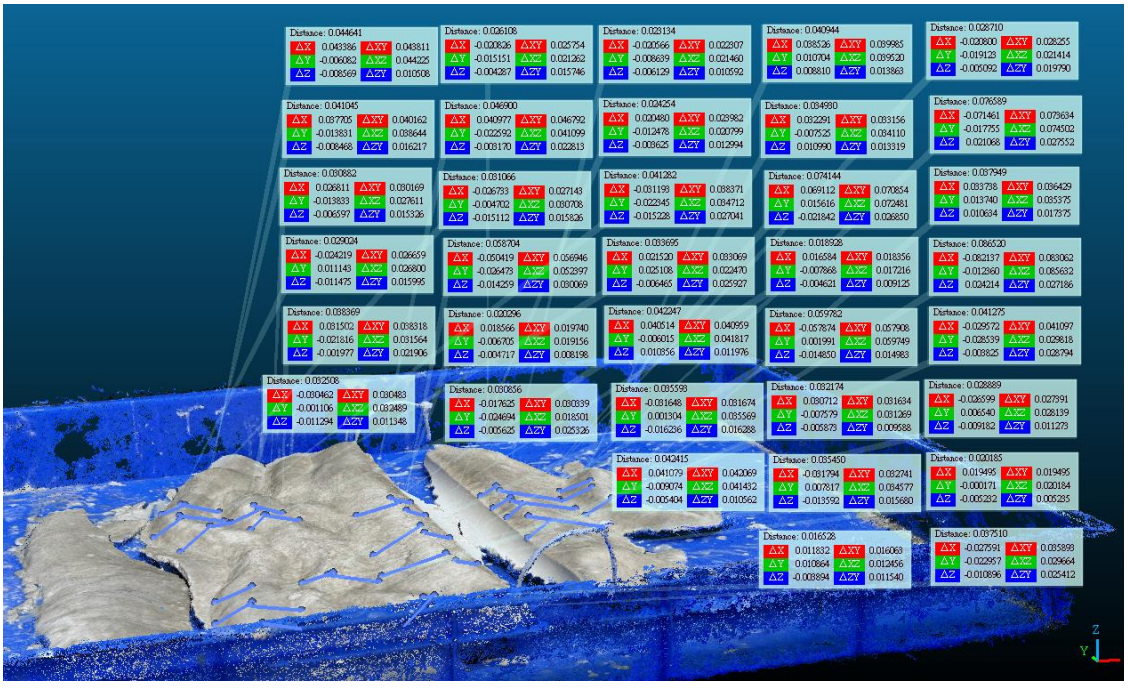

Figure 4.34 Sand ripple height data points of d90 h50 e2.5

doi:10.6342/NTU202404035

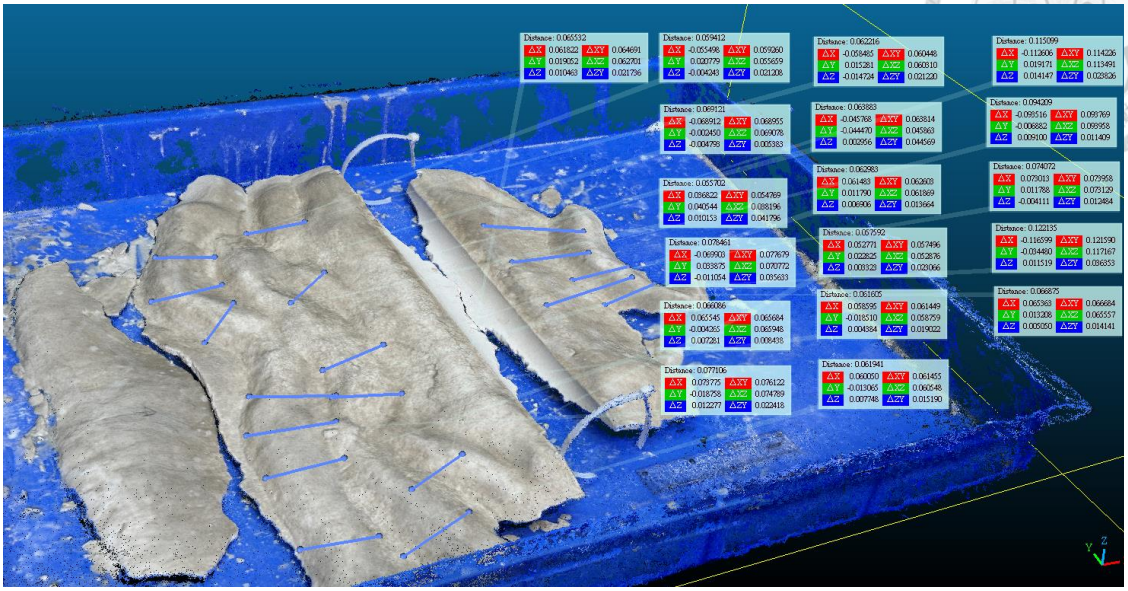

Figure 4.35 Wavelength data points of d90 h50 e2.5

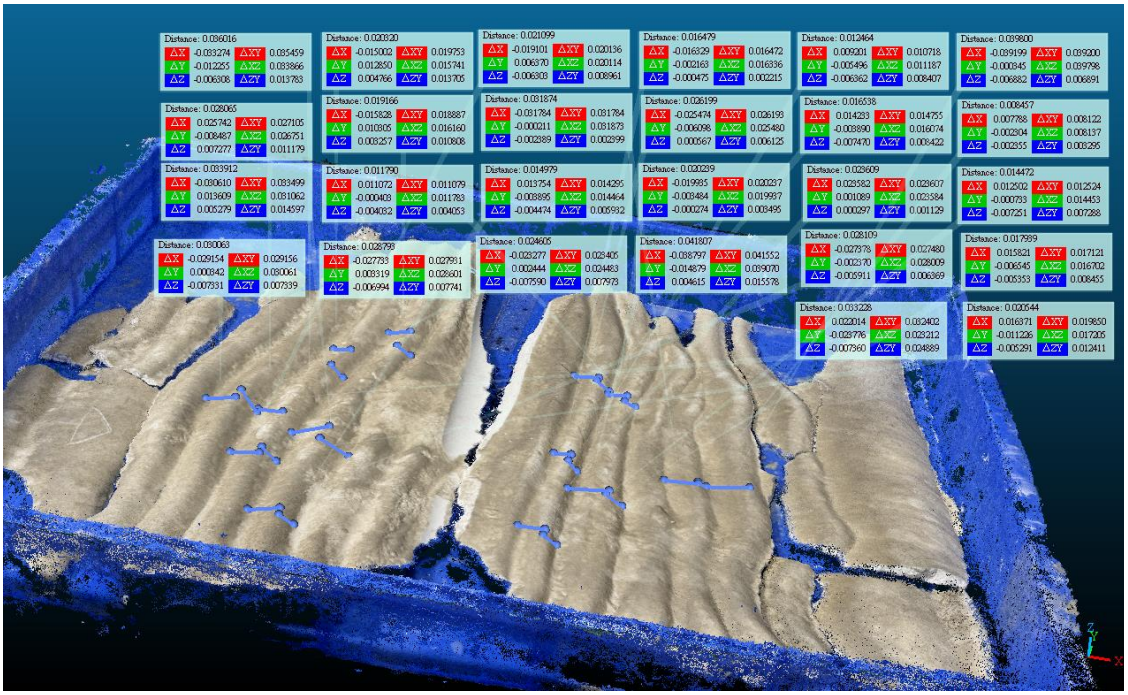

Figure 4.36 Sand ripple height data points of d90 h40 e2.5

doi:10.6342/NTU202404035

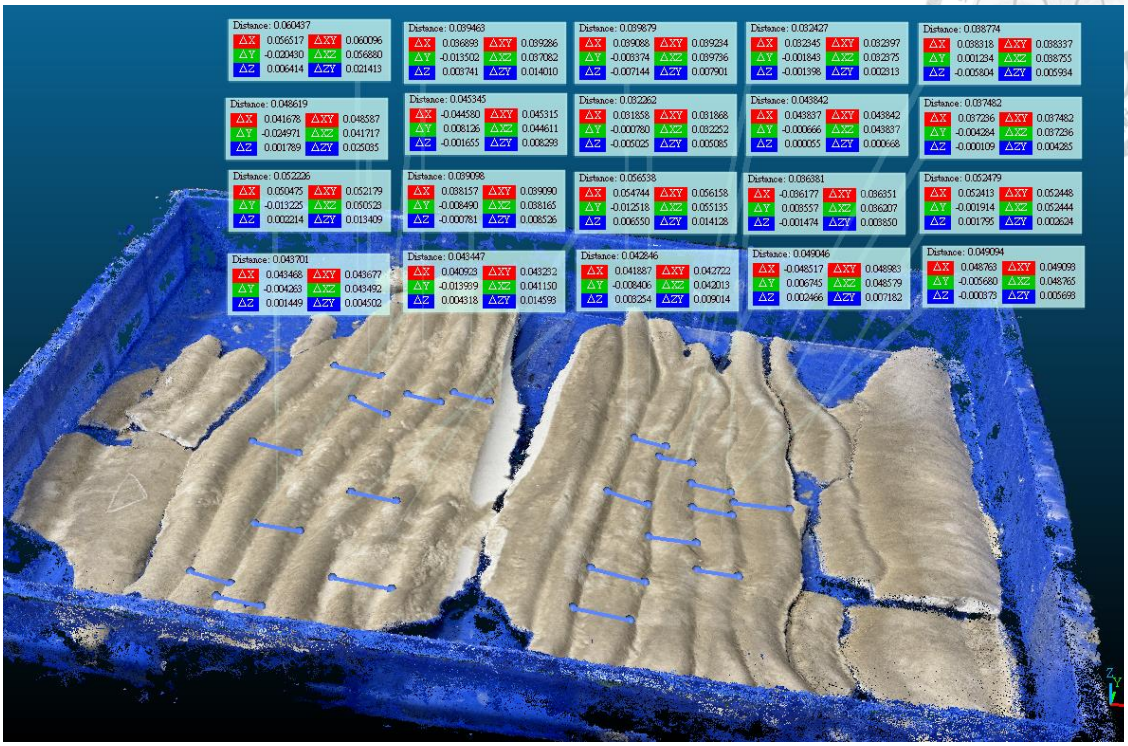

Figure 4.37 Wavelength data points of d90 h40 e2.5

doi:10.6342/NTU202404035

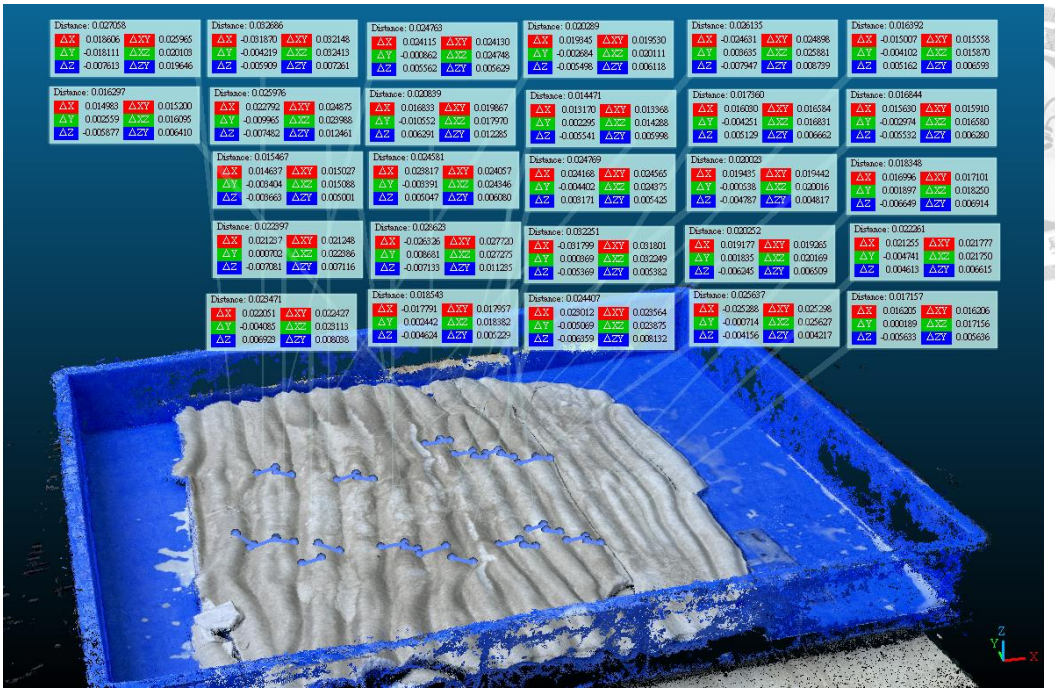

Figure 4.38 Sand ripple height data points of d90 h40 e5

doi:10.6342/NTU202404035

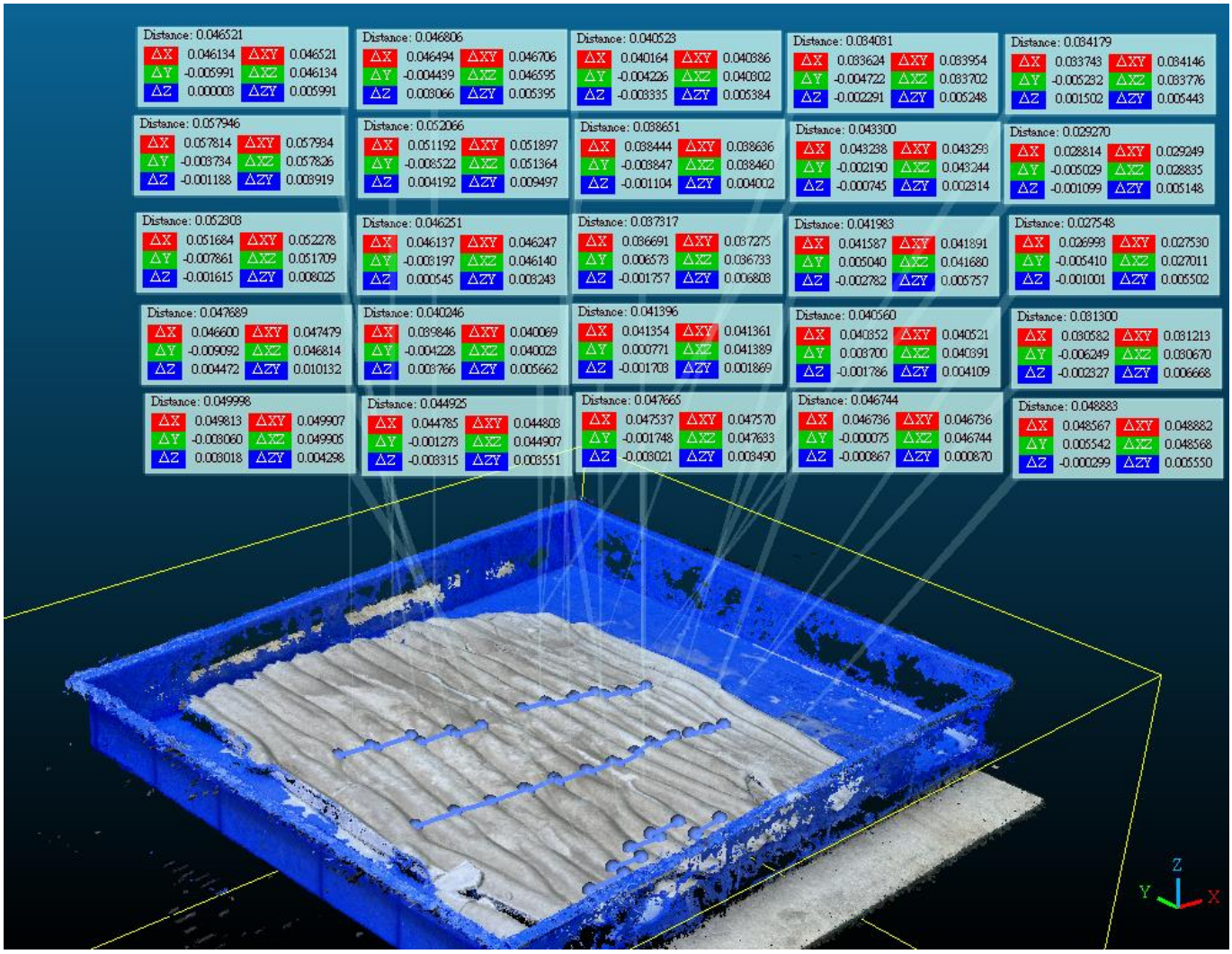

Figure 4.39 Wavelength data points of d90 h40 e5

doi:10.6342/NTU202404035

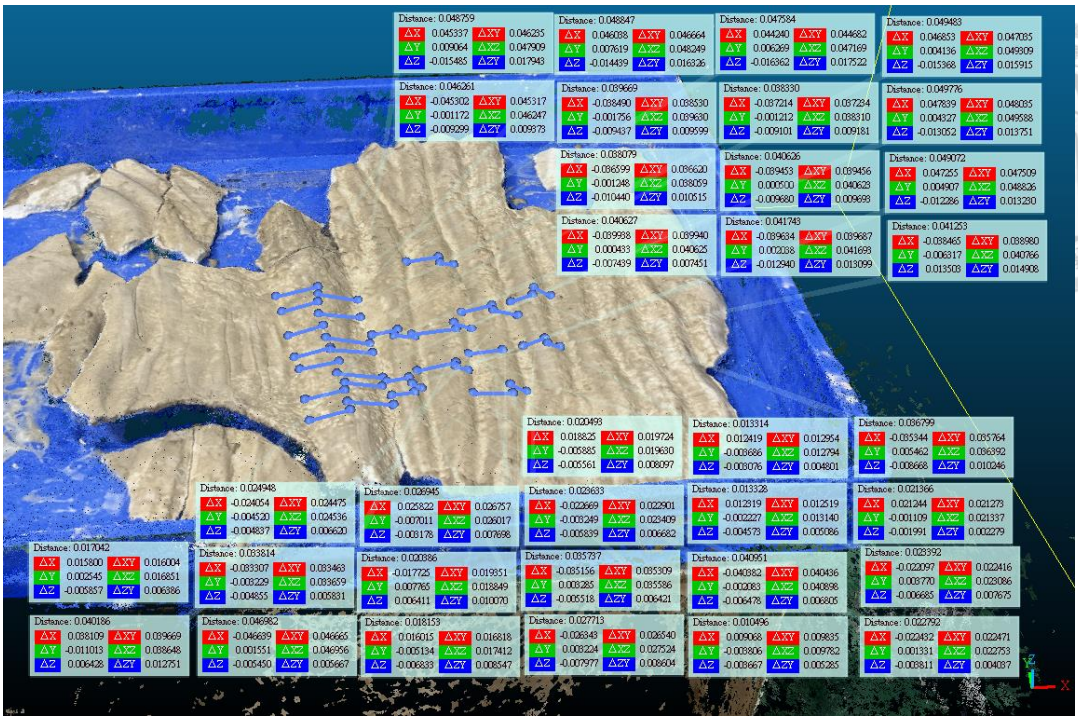

Figure 4.40 Sand ripple height and scour depth data points of d90 h40 e0

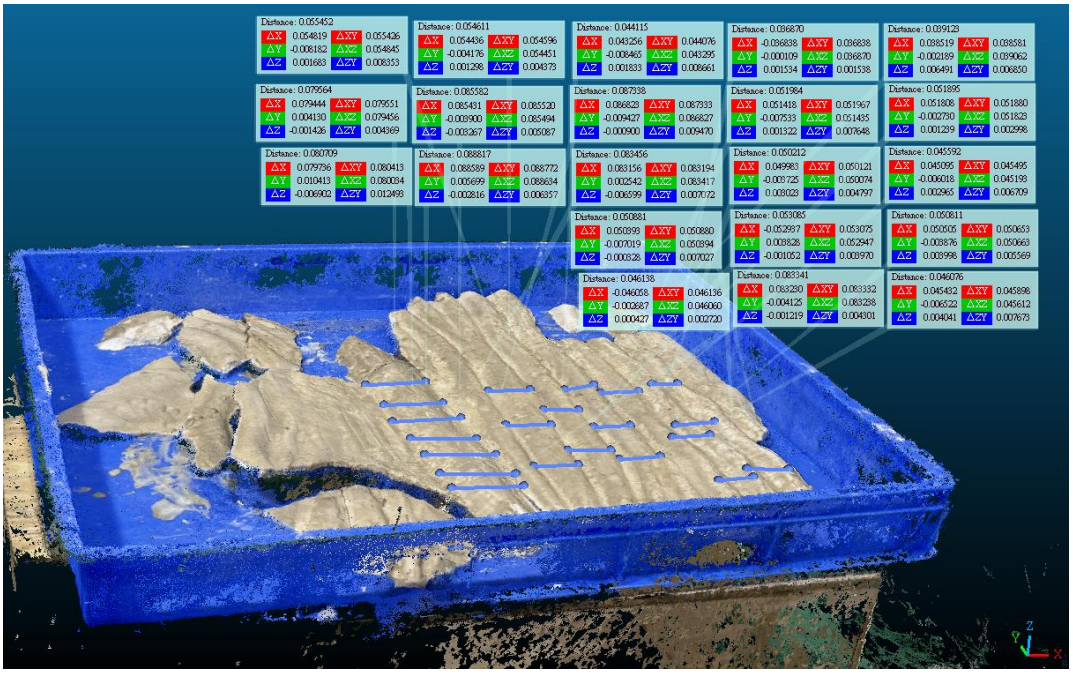

Figure 4.41 Wavelength and scour width data points of d90 h40 e0

doi:10.6342/NTU202404035

Chapter 5 Conclusions and Recommendations

5.1 Conclusions

Based on the flume tests and close-range photogrammetry analysis results, the following conclusions are drawn:

(1) The scouring depth and characteristics of the sand ripples (in terms of ripple amplitude and frequency) are consistent with the experimental observations by other researchers.

(2) The scour cannot be observed around the pipes oriented parallel to the wave propagation direction.

(3) Scour would occur when the pipelines were not buried. Based on past research, scour could occur if the buried depth is less than the diameter of the pipeline. However, , scour did not occur in this study for the half-buried pipelines because the Keulegan-Carpenter number criterion was not met.

(4) The relationship between scour depth and pipeline orientation as implied from this study follows a similar trend to that from other researcher.

(5) Based on past studies by other researchers, as water depth gets larger, the wavelength of the ripple would be shorter. However, an opposite trend was observed in this study..

doi:10.6342/NTU202404035

5.2 Recommendations for Future Research

As this series of experiments is our first attempt to study scour around pipelines, a lot of improvements can be made for future studies:

1. The boundary of the sandbox had a huge impact on the experimental results. It can be found that a huge sand pit was formed behind the side of the wooden box that first made contact with the waves. Its existence may affect the motion state of the water particles. The sandbox seems not fitting perfectly into the sink area of the flume.

2. The sandbox deformed gradually as more experiments were conducted. Other materials should be considered for future sandbox.

3. For the wave-amplitude considered in this study, the wave-maker can only produce waves with frequency of 0.8 Hz, which makes it difficult for the scour to occur. The wave-maker may need adjustment such that wave with larger amplitude or higher frequency can be produced.

doi:10.6342/NTU202404035

Reference

[1] Bayraktar, D., Ahmad, J., Larsen, B. E., Carstensen, S., & Fuhrman, D. R. (2016). Experimental and numerical study of wave-induced backfilling beneath submarine pipelines. Coastal Engineering, 118, 63–75.

[2] Çevik, E., & Yüksel, Y. (1999). Scour under submarine pipelines in waves in shoaling conditions. Journal of Waterway, Port, Coastal, and Ocean Engineering, 125(1), 9–19.

[3] Dogan, M., & Arisoy, Y. (2015). Scour regime effects on the time scale of wave scour below submerged pipes. Ocean Engineering, 104, 673–679.

[4] Etemad-Shahidi, A., Yasa, R., & Kazeminezhad, M. H. (2011). Prediction of wave-induced scour depth under submarine pipelines using machine learning approach. Applied Ocean Research, 33(1), 54–59.

[5] Jeng, D.-S., & Cheng, L. (2000). Wave-induced seabed instability around a buried pipeline in a poro-elastic seabed. Ocean Engineering, 27(2), 127–146.

[6] Kim, S., Lee, H.-J., & Yeon, J.-H. (2011). Characteristics of parameters for local scour depth around submarine pipelines in waves. Marine Georesources & Geotechnology, 29(2), 162–176.

doi:10.6342/NTU202404035

[7] Liang, W., Lou, M., Fan, C., Zhao, D., & Li, X. (2023). Coupling effect of vortex-induced vibration and local scour of double tandem pipelines in steady current. Ocean Engineering, 286, 115495.

[8] Li, B., & Ma, H. (2022). Scouring mechanism of suspended and partially-buried pipelines under Steady Flow. Coastal Engineering, 177, 104201.

[9] Lin, J., Jeng, D.-S., Zhao, H., Gao, Y., Liu, J., & Guo, Y. (2023). Recent advances of seabed liquefaction around the vicinity of marine structures. Ocean Engineering, 280, 114660.

[10] Luhmann, T. (2010). Close range photogrammetry for Industrial Applications. ISPRS Journal of Photogrammetry and Remote Sensing, 65(6), 558–569.

[11] Ma, H., Li, B., & Zhang, S. (2024). Scour mechanism around a pipeline under different current-wave conditions using the CFD-dem coupling model. Computers and Geotechnics, 170, 106304.

[12] Mattioli, M., Mancinelli, A., & Brocchini, M. (2013). Experimental investigation of the wave-induced flow around a surface-touching cylinder. Journal of Fluids and Structures, 37, 62–87.

doi:10.6342/NTU202404035

[13] Marini, F., Postacchini, M., Pizzigalli, C., Badalini, M., Corvaro, S., & Brocchini, M. (2023). On the onset of pipeline scouring: Reconciling waves and currents forcing. SSRN Electronic Journal.

[14] Mohr, H., Draper, S., Cheng, L., & White, D. J. (2016). Predicting the rate of scour beneath subsea pipelines in marine sediments under steady flow conditions. Coastal Engineering, 110, 111–126.

[15] Mousavi, M. E., Bakhtiary, A. Y., & Enshaei, N. (2009). The equivalent depth of wave-induced scour around offshore pipelines. Journal of Offshore Mechanics and Arctic Engineering, 131(2).

[16] Mousavi, M. E., Yeganeh Bakhtiary, A., & Enshaei, N. (2006). The equivalent depth of wave-induced scour around offshore pipelines. Volume 1: Offshore Technology; Offshore Wind Energy; Ocean Research Technology; LNG Specialty Symposium.

[17] Nielsen, P. (1981). Dynamics and geometry of wave-generated ripples. Journal of Geophysical Research: Oceans, 86(C7), 6467–6472.

[18] Pu, Q., Li, K., Gao, F., (2001). Scour of the seabed under a pipeline in oscillating flow. China Ocean Eng. 15 (1), 129–138.

[19] Qi, W.-G., Li, C.-F., Jeng, D.-S., Gao, F.-P., & Liang, Z. (2019). Combined wave-current induced excess pore-pressure in a sandy seabed: Flume observations and

doi:10.6342/NTU202404035

comparisons with theoretical models. Coastal Engineering, 147, 89–98.

[20] Rieke-Zapp, D., Tecklenburg, W., Peipe, J., Hastedt, H., & Haig, C. (2009). Evaluation of the geometric stability and the accuracy potential of digital cameras — comparing mechanical stabilisation versus parameterisation. ISPRS Journal of Photogrammetry and Remote Sensing, 64(3), 248–258.

[21] Soulsby, R. L., Whitehouse, R. J. S., & Marten, K. V. (2012). Prediction of time-evolving sand ripples in shelf seas. Continental Shelf Research, 38, 47–62.

[22] Soulsby, Richard L., & Whitehouse, R. J. (2005). Prediction of ripple properties in shelf seas. mark 2 predictor for Time Evolution. Defense Technical Information Center.

[23] Sumer, B. M., & Kirca, V. S. (2022). Scour and liquefaction issues for anchors and other subsea structures in floating offshore wind farms: A Review. Water Science and Engineering, 15(1), 3–14.

[24] Sumer, B Mutlu, & Fredsøe, J. (2002). The mechanics of Scour in the marine environment. Advanced Series on Ocean Engineering.

[25] Sumer, B. M., Truelsen, C., Sichmann, T., & Fredsøe, J. (2001). Onset of scour below pipelines and self-burial. Coastal Engineering, 42(4), 313–335.

[26] Sumer, B. M., & Fredsøe, J. (1991). Scour below pipelines in waves. Journal of

doi:10.6342/NTU202404035

Waterway, Port, Coastal, and Ocean Engineering, 116(3), 307–323.

[27] Sharafati, A., Yasa, R., & Azamathulla, H. M. (2018). Assessment of stochastic approaches in prediction of wave-induced pipeline scour depth. Journal of Pipeline Systems Engineering and Practice, 9(4).

[28] Teh, T. C., Palmer, A. C., & Damgaard, J. S. (2003). Experimental study of marine pipelines on unstable and liquefied seabed. Coastal Engineering, 50(1–2), 1–17.

[29] Vittori, G., & Blondeaux, P. (2024). On the prediction of the characteristics of sand ripples at the bottom of sea waves. Earth-Science Reviews, 252, 104753.

[30] Zang, Z., Tang, G., Chen, Y., Cheng, L., & Zhang, J. (2019). Predictions of the equilibrium depth and time scale of local scour below a partially buried pipeline under oblique currents and waves. Coastal Engineering, 150, 94–107.

[31] Zang, Z., Cheng, L., Zhao, M., Liang, D., & Teng, B. (2009). A numerical model for onset of scour below offshore pipelines. Coastal Engineering, 56(4), 458–466.

[32] Zhai, Y., Zhang, J., Guo, Y., Tang, Z., & Zhang, T. (2022). Study of wave-induced seabed response around twin pipelines in sandy seabed through laboratory experiments and numerical simulations. Ocean Engineering, 244, 110344.

[33] Zhang, Y., Wu, J., Zhang, S., Li, G., Jeng, D.-S., Xu, J., Tian, Z., & Xu, X. (2022).

doi:10.6342/NTU202404035

An optimal statistical regression model for predicting wave-induced equilibrium scour depth in sandy and silty seabeds beneath pipelines. Ocean Engineering, 258, 111709.

[34] Zhang, Q., Draper, S., Cheng, L., & An, H. (2016). Effect of limited sediment supply on sedimentation and the onset of tunnel scour below subsea pipelines. Coastal Engineering, 116, 103–117.

[35] 陳莉妏 (2010)，重力水波下之粒子運動軌跡及質量傳輸之研究，碩士論文，國立台灣大學。

doi:10.6342/NTU202404035